Cement and Concrete Research 42 (2012) 686–699

Contents lists available at SciVerse ScienceDirect

Cement and Concrete Research

journal homepage: http://ees.elsevier.com/CEMCON/default.asp

# Differential-scheme based dissolution/diffusion model for calcium leaching in cement-based materials accounting for mix design and binder composition

Ch. Pichler *, A. Saxer, R. Lackner

*Material Technology Innsbruck (MTI), University of Innsbruck, Technikerstraße 13, A-6020 Innsbruck, Austria*

ARTICLE INFO

*Article history:*
Received 6 June 2011
Accepted 15 February 2012

*Keywords:*
Diffusion (C)
Electrochemical properties (C)
Transport properties (C)
$Ca(OH)_2$ (D)
Calcium leaching

ABSTRACT

A material model for calcium dissolution/diffusion in cement-based materials is presented, taking the increase of porous space due to calcium leaching into account. The so-called differential-scheme is employed to link the underlying effective diffusive properties to the pore-space volume. The so-obtained material description is used within an analysis scheme based on the finite element method for the simulation of calcium dissolution/diffusion processes at the macroscopic scale. The re-analysis of leaching tests on cement-paste specimens in deionized water and ammonium nitrate solution, respectively, in terms of the rise in calcium concentration in the sample-enclosing aggressive solution, is used for assessment of underlying model assumptions, such as the material function relating calcium concentration bound in solid material skeleton to calcium concentration in the pore fluid. Moreover, the diffusion coefficient of the electrolyte solution in the pore space of cement-based materials, serving as input for determination of the effective diffusion properties, is investigated.



## 1. Introduction

Calcium leaching is a severe chemical softening mechanism in cement-based materials characterized by a significant increase of porosity, leading to substantial stiffness and strength loss (see, e.g., [1]) accompanied by an increase of pore pressure sensitivity [2,3]. There are numerous papers dealing with durability of cement-based materials as regards this mode of chemical softening (by deionized water), see, e.g., [4–18,1,2,19–25]. Hereby, instantaneous dissolution of calcium bound in the solid skeleton and Fick-type diffusion of calcium ions in the pore solution are considered. The diffusion tensor $\mathbf{D}_{\text{eff}}$ [$dm^2/h$], characterizing the macroscopic material behavior, with $\mathbf{D}_{\text{eff}} = D_{\text{eff}}\mathbf{I}$ in case of material isotropy, may be determined

- by empirical relations, e.g., $D_{\text{eff}} = exp(a\phi)\bar{D}$ [12], with $a$ [–] and $\bar{D}$ [$dm^2/h$] representing fitting parameters obtained from backcalculation of macroscopic data and $\phi$ [$dm^3/(dm^3$ concrete)] denoting the connected pore space saturated with pore solution, or
- from the diffusion coefficient of the solute in the interstitial pore solution $D_{\text{sol}}$ by volumetric averaging $D_{\text{eff}} = \phi D_{\text{sol}}$ (see, e.g., [20]),
- numerical homogenization schemes giving $D_{\text{eff}} = D_{\text{eff}}(D_{\text{sol}}, \phi)$, see, e.g., [22] for a two-scale approach considering triangular or spherical inclusions in a matrix material, i.e., a two-phase representation of concrete.
- homogenization schemes based on continuum micromechanics providing $D_{\text{eff}} = D_{\text{eff}}(D_{\text{sol}}, \phi)$, e.g., two-scale representation based on the differential scheme [26,27] or multiscale representation based on the composite sphere assembly method [28–32].

As regards the underlying material function describing the equilibrium state, relating the calcium concentration in the pore solution $c$ [mol/(l solution)] to the (apparent) calcium concentration bound in the solid skeleton $s$ [mol/($dm^3$ concrete)], a phenomenological approach based on dissolution data of synthesized C–S–H[1] prepared at different C/S molar ratios collected by [33] (see Fig. 1(a)) is commonly employed in the literature (see, e.g., [18,12,20,21]), giving $s = s(c)$. In [34–36] a leaching kinetics law originally proposed by [18] is employed, with the previously mentioned equilibrium curve serving as the limiting dissolution state, allowing a more realistic modeling of calcium dissolution from the solid skeleton upon a fast calcium concentration decrease in the pore fluid. Recently, [37] conducted experiments fitting well within the data summarized in [33]. Assuming (i) local thermodynamic equilibrium and (ii) that the Si-concentration in the solid remains constant, an equilibrium function giving the Ca-concentration in the dissolved solid $s$ as a function of the Ca-concentration in the aqueous solution $c$ is obtained (originally proposed by [5,7], see Fig. 1(b)). The equilibrium function has been interpreted such that with decreasing Ca-concentration $c$,

- portlandite CH ($\sim 0.020$ mol/l$< c < c^{eq}$),

* Corresponding author.
*E-mail address:* christian.pichler@uibk.ac.at (C. Pichler).

[1] Standard cement chemistry abbreviations are used throughout this paper: C = CaO, S = $SiO_2$, A = $Al_2O_3$, F = $Fe_2O_3$, $\bar{S}$ = $SO_3$, H = $H_20$.

0008-8846/$ – see front matter © 2012 Elsevier Ltd. All rights reserved.
doi:10.1016/j.cemconres.2012.02.007

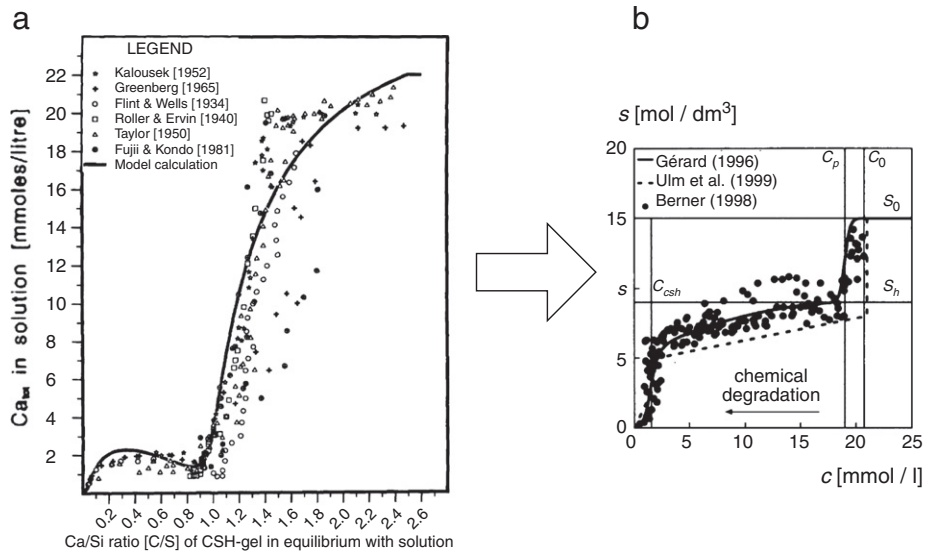


**Fig. 1.** (a) Dissolution data collected and analyzed by [33], figure taken from [33] and (b) equilibrium function proposed by [5,7] and used in numerical analyzes by [20,21], figure taken from [20] with the calcium concentration in the pore solution $c$ given in [mmol/l] and the calcium concentration in the dissolved solid $s$ given in [mol/dm$^3$].

- sulfoaluminates (monosulfate and ettringite) ($\sim 0.002$ mol/l$< c <\sim 0.020$ mol/l), and
- C–S–H ($0 < c <\sim 0.002$ mol/l)

are dissolved/decalcified subsequently from the solid skeleton (see, e.g., [20]), with the equilibrium calcium concentration of a solution saturated in CH as $c^{eq} = 0.022$ mol/l. Experimental evidence by XRD and SEM investigations, validating this sequential dissolution/decalcification of the listed calcium-bearing hydration products (in the order CH, monosulfate, ettringite, and C–S–H) can be found in [4] (see also Fig. 1 in [18]), with the chemically softened region composed of four zones with quasi-constant mineralogy. This characteristic equilibrium function (with a steep increase at $c \sim 0.002$ mol/l attributed to the dissolution of Ca from C–S–H) has been used in most publications dealing with numerical simulation of calcium leaching (see, e.g., [18,12,20,21,34–36]).

In this paper, the porous space associated to the various leaching states is taken into account within the framework of non-periodic homogenization schemes. Hereby, in an engineering approach, simple analytical homogenization schemes based on continuum micromechanics [26,38,39] are assessed, and finally the differential scheme is employed for determination of the diffusion coefficient characterizing the macroscopic material behavior, $D_{\text{eff}}$.

The paper is structured as follows: in the following section, the model for determination of diffusive properties is presented, including comments on the interstitial electrolyte diffusion coefficient serving as input for the homogenization scheme. In Section 3, the material model is used in a finite element program for the simulation of calcium dissolution/diffusion, allowing the re-analysis of leaching tests in both deionized water and in ammonium-nitrate solution (accelerated leaching), respectively. These analyses will provide the basis for the assessment of basic model assumptions, such as the equilibrium function shown in Fig. 1(b) and the underlying diffusion coefficient of the electrolyte solution introduced in Section 2.

## 2. Estimation of effective diffusion coefficient

### *2.1. Hydration stoichiometry model for initial composition of material system*

The following set of stoichiometric reactions are employed for the four main clinker phases of Portland cement, i.e., tricalcium silicate ($C_3S$), dicalcium silicate ($C_2S$), tricalcium aluminate ($C_3A$), and tetracalcium aluminate ferrite ($C_4AF$) [40]:

$$C_3S + 5.3H \rightarrow 0.5C_{3.4}S_2H_8 + 1.3CH \quad (1)$$

$$C_2S + 4.3H \rightarrow 0.5C_{3.4}S_2H_8 + 0.3CH \quad (2)$$

$$C_4AF + 2CH + 10H \rightarrow 2C_3(A,F)H_6 \quad (3)$$

$$C_3A + 3C\bar{S}H_2 + 26H \rightarrow C_6A\bar{S}_3H_{32} \quad (4)$$

$$C_3A + 0.5C_6A\bar{S}_3H_{32} + 2H \rightarrow 1.5C_4A\bar{S}H_{12} \quad (5)$$

$$C_3A + CH + 12H \rightarrow C_4AH_{13} \quad (6)$$

Eqs. (4) to (6) describe the subsequent formation of calcium aluminate hydrates from $C_3A$ in the presence of gypsum, which is added to prevent rapid setting of $C_3A$. Initially, $C_3A$ reacts with gypsum to form ettringite [Eq. (4)]. After all gypsum is consumed, $C_3A$ reacts with the previously formed ettringite to form monosulfoaluminates [Eq. (5)]. Following depletion of the ettringite supply, $C_3A$ reacts with portlandite CH (one of the products of $C_3S$ and $C_2S$ hydration).

Eqs. (1) to (6) combined with the molar masses and densities of material phases given in [40] (see Table B.4 in Appendix B) and the mix design, i.e. $w/c$-ratio, aggregate/cement-ratio, and aggregate density provide access to the volume fractions of the phases in cement paste, mortar or concrete, for details see [41]. In addition to the solid material phases (hydration products), the stoichiometry model predicts a value for the capillary pore space, i.e., the space not occupied by hydration products and aggregates. This value is mainly influenced by the value employed for the saturated C–S–H density. The latter is associated to Jennings colloidal C–S–H model [42–45] with the largest gel pores in the C–S–H gel approximately 20 nm wide ([45], page 282). Accordingly, the capillary pore space estimated in this paper may be characterized by pore widths of $>20$ nm.

### *2.2. Methodology for micro-to-macro transition based on classical schemes from continuum micromechanics*

As regards upscaling of the diffusive transport properties of heterogeneous, non-periodic media, analytical homogenization schemes

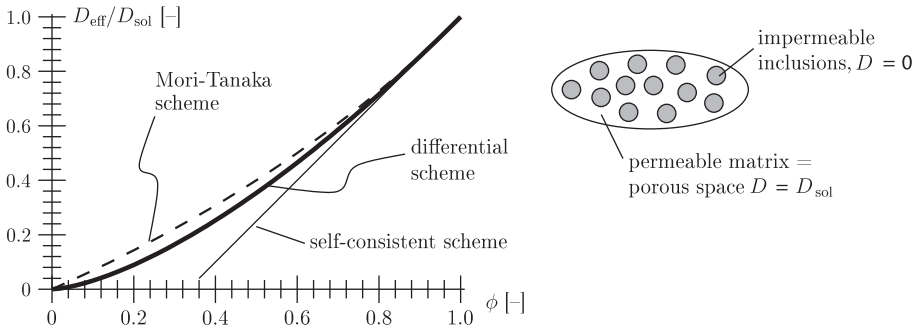


**Fig. 2.** Homogenization schemes for effective diffusion properties of a two-phase medium.

based on continuum micromechanics (derived for upscaling of elastic properties) may be employed due to the similarities in the underlying field equations. Fig. 2 shows results for a two-phase medium consisting of (i) a continuous, permeable matrix, representing the saturated, connected porous space in the material system, and (ii) impermeable inclusions [39,38]. Considering spherical inclusions and a connected pore space (volume fraction $\phi$),

- the Mori–Tanaka scheme [46],[2] equivalent to the Hashin–Shtrikman upper bound, yields the effective diffusion coefficient as [26]

$$D_{eff} = D_{sol}\frac{2\phi}{3-\phi}; \tag{7}$$

- the self-consistent scheme [47,48][3] gives [38]

$$D_{eff} = D_{sol}\frac{3\phi-1}{2} \quad \text{for} \quad \phi \geq 1/3; \quad D_{eff} = 0 \quad \text{for} \quad \phi < 1/3; \tag{8}$$

- the so-called differential scheme [49,26][4] represents an incremental formulation of the self-consistent scheme, with

$$D_{eff} = D_{sol}\phi^{3/2}. \tag{9}$$

The pore-space dependent part of the relations for the effective diffusion coefficient are classically split into two multipliers accounting for (i) the respective value of the pore space $\phi$ and (ii) the so-called tortuosity $T_\phi$ capturing the effect of the geometry of the microstructure [38], i.e.,

$$D_{eff}/D_{sol} = \phi T_\phi, \tag{10}$$

giving, e.g., the tortuosity for the differential scheme as $T_\phi = \phi^{1/2}$.

All three homogenization schemes presented above coincide for $\phi \to 1$, with $\partial(D_{eff}/D_{sol})/\partial\phi|_{\phi=1} = 3/2$. Hence, for $\phi \to 1$ the response of the non-periodical homogenization schemes can be written as $D_{eff}/D_{sol} = (3\phi-1)/2 = \phi T_\phi$ (see Eq. (8)). The respective tortuosity is given as

$$T_{\phi\to 1} = \frac{3}{2} - \frac{1}{2\phi} = 1, \tag{11}$$

i.e., no 'detours' imposed by the geometry of the microstructure, which eventually vanishes for $\phi \to 1$.

The prediction for the effective diffusion coefficient for small values of $\phi$ is quite different, with the self-consistent scheme giving an effective value for the diffusion coefficient only for $\phi$ exceeding a percolation threshold of 1/3. In case of the differential scheme, $D_{eff}/D_{sol}$ has a horizontal tangent at $\phi = 0$, whereas the Mori–Tanaka scheme yields $\partial(D_{eff}/D_{sol})/\partial\phi|_{\phi=0} = 2/3$. Accordingly, in the range of the small values for the porosity $\phi$, such as that encountered in mortar or concrete, the Mori–Tanaka scheme (coinciding with the Hashin–Shtrikman upper bound for spherical inclusions) may significantly underestimate $D_{sol}$ assessed based on a experimentally determined $D_{eff}$.[5] On the other hand, for a given value of $D_{sol}$, the Mori–Tanaka scheme may significantly overestimate the tortuosity and, thus, the effective diffusion coefficient in this porosity range [26,32].

Finally, when employing the volumetric average for the effective diffusivity, i.e., $D_{eff} = \phi D_{sol}$, hence, underlying $T_\phi = 1$, the Hashin–Shtrikman upper bound is violated (for the considered pore space configuration). In case of the theoretical case of parallel pores with constant cross-sectional area of the individual pores, the latter estimation is adequate.

Within this paper, the differential scheme is employed to link the effective diffusion coefficient of cement based materials $D_{eff}$ to the interstitial diffusion coefficient $D_{sol}$ representing the material behavior within the porous space of the material. For the situation encountered for cement-based materials under chemical attack (by deionized water or 6 M $NH_4NO_3$ solution) investigated in this paper, characterized by a rapid increase of the porous space by dissolution of CH, decalcification of sulfoaluminates, etc. in the zone where the ionic transport is taking place, the differential scheme may provide an adequate engineering tool to assess the transport behavior of the chemically softened materials investigated, which are, furthermore, characterized by $w/c \geq 0.5$, i.e., by a large value for the initial capillary pore space. In this paper, percolation of the initial pore space is assumed to be established by "pore families" with widths < 200 nm[6] (see [32] and references therein).

### 2.3. Additional porosity caused by chemical degradation

Whereas the additional capillary pore space due to complete dissolution of CH, $\phi_{CH}^{max}$, is straight-forwardly estimated as the initial

[2] The Mori–Tanaka may be employed for matrix/inclusion-type morphologies with moderate values for the inclusion volume fraction of $<\sim 0.2$.

[3] The self-consistent scheme is best-suited for microstructures where none of the material phases plays a specific morphological role, such as, e.g., in polycrystals.

[4] The model configuration for the self-consistent scheme is characterized by the consideration of the different material phases as inclusion surrounded by the homogenized medium. The differential scheme represents an incremental formulation of the self-consistent scheme: consideration of a homogeneous medium embedding an inclusion phase with infinitesimal increase of the volume fraction of the latter. After each incremental increase the effective material behavior, i.e., the behavior of the embedding material phase, is updated using the result of the micromechanical homogenization scheme for dilute defect distributions [39].

[5] Suppose a macroscopic experiment gives access to $D_{eff}$ of a porous material and the Mori–Tanaka scheme and the differential scheme, respectively, are used to identify $D_{sol}$. Considering the right hand sides of Eqs. (7) and (9) gives $D_{sol}^{MT} = [\phi^{1/2}(3-\phi)/2]D_{sol}^{DS}$. Hence, e.g., for $\phi = 0.1$, $D_{sol}$ determined by the Mori–Tanaka scheme amounts to 45.9% of the value determined by the differential scheme, $D_{sol}^{MT} = 0.459 D_{sol}^{DS}$. For $\phi = 0.2$: $D_{sol}^{MT} = 0.626 D_{sol}^{DS}$, and for $\phi = 0.3$: $D_{sol}^{MT} = 0.739 D_{sol}^{DS}$.

[6] According to [32] (and references therein) only "pore families" with width < 200 nm form a percolation path through the material system. These "pore families" are denoted as gel porosity in [32]; note this width was defined in [32] and does not necessarily represent gel porosity in the scopes of Jennings model (see Section 1); the porosity denoted as capillary porosity in this paper includes "pore families" with width > 20 nm, hence, is percolated throughout the material system.

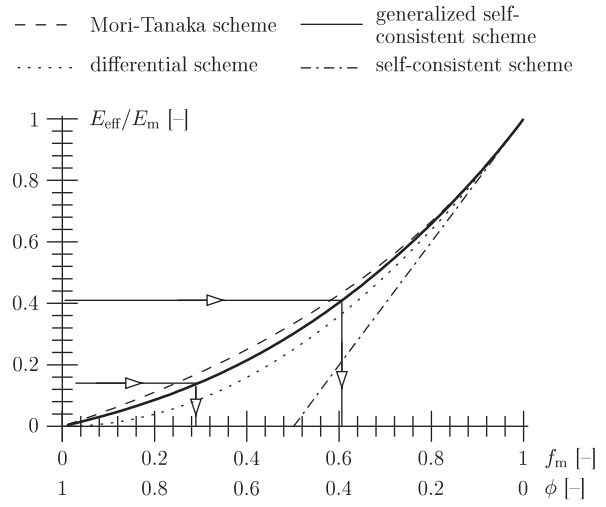


**Fig. 3.** Results from different homogenization schemes for Young's modulus of a porous medium.

volume fraction of CH, the assessment of the additional pore space due to C–S–H decalcification, $\phi_{C-S-H}^{max}$, is more complex. In this paper, nanoindentation results on intact and completely decalcified cement-paste samples presented in [50] are employed. Hereby, Young's modulus $E$ of the two material phases, low-density C–S–H (C–S–H-LD) and high-density C–S–H (C–S–H-HD), constituting C–S–H in the cement-based material system, amount to 21.7 and 29.4 GPa, respectively. After calcium leaching, Young's modulus decreased to 14% (C–S–H-LD) and 41% (C–S–H-HD) of the initial values. Fig. 3 shows results from classical homogenization schemes based on continuum micromechanics for a porous medium (spherical pores), with $f_m$ and $E_m$ denoting the volume fraction and Young's modulus of the matrix material. Poisson's ratio of the latter was set to $\nu_m = 0.24$ (value for C–S–H, see [50]). Employing the generalized self-consistent scheme [51,52], the porous material with an effective Young's modulus, $E_{eff}$, of 14% of $E_m$ is characterized by $f_m = 0.29$, hence yields a porosity of $\phi = 1 - f_m = 0.71$ for decalcified C–S–H-LD (see Fig. 3). For $E_{eff}/E_m = 41\%$, the porosity results in $\phi = 0.39$ for decalcified C–S–H-HD. Considering volume fractions of C–S–H-LD and C–S–H-HD in C–S–H as 0.7 and 0.3 [50,40], respectively, the overall porosity after complete C–S–H decalcification is estimated as $\bar{\phi}_{C-S-H}^{max} = 0.7 \times 0.71 + 0.3 \times 0.39 = 0.6$. In contrast to the microstructural representation employed for estimating effective diffusive properties (Subsection 2.2), the percolated material phase is assigned to the solid material phase. None of the classical homogenization schemes for non-periodic media seems to satisfactorily capture both (i) transport properties and (ii) mechanical properties of cement-based materials when underlying the identical microstructural representation. This may be explained by the colloidal nature of C–S–H gel [42–45] [and probably (partially) decalcified C–S–H gel].

### 2.4. Determination of $D_{sol}$ in bulk aqueous solution

The molar conductivity $\Lambda_m = \kappa/c$ [Sm$^2$/mol], where the conductivity $\kappa$ [S/m] is scaled by the molar concentration[7] of dilute solutions of strong electrolytes varies linearly with the square root of the electrolyte concentration $c$ according to Kohlrausch's law (empirical relation)

$$\Lambda_m = \Lambda_m^0 - \mathcal{K}\sqrt{c}, \tag{12}$$

where the constant $\mathcal{K}$ depends more on the stoichiometry of the electrolyte than on its specific identity [53]. In Eq. (12), $\Lambda_m^0$ is the limiting molar conductivity for zero concentration, which is given by Kohlrausch's law of independent migration of ions, reading

$$\Lambda_m^0 = \nu_+ \lambda_+^0 + \nu_- \lambda_-^0, \tag{13}$$

where $\lambda_+^0(\lambda_-^0)$ is the molar conductivity of the cation (anion) at zero ion concentration, and $\nu_+(\nu_-)$ is the number of cations (anions) per stoichiometric unit of the electrolyte (see Table 1 for some investigated electrolytes). $\lambda_+^0(\lambda_-^0)$ is determined based on the elementary charge $z_+(z_i)$ of the cation (anion) and the so-called ionic mobility $u_+(u_-)$ of the respective ion as

$$\lambda_\pm^0 = z_\pm u_\pm F, \tag{14}$$

with $F$ denoting the Faraday constant (see Table B.5 in Appendix B). The ionic mobility characterizes the ionic motion in an electric field (i.e., of cations towards the negative electrode and of anions towards the positive electrode) which is retarded by frictional forces. Hence, $u_\pm$ is inversely proportional to the radius $a$ of the cation (anion) and the viscosity of water[8] $\eta$ [Pa s] [53]:

$$u_\pm = \frac{z_\pm e}{6\pi\eta a}, \tag{16}$$

where $e$ is the elementary charge (see Table B.5 in Appendix B).

Kohlrausch's phenomenological law (Eq. (12)) is improved by the Debye–Hückel–Onsager theory, taking into account the reduction of ionic mobility by ion–ion interaction, i.e.,

- by the so-called relaxation effect (distortion of the spherical symmetric ionic atmosphere when an electric field is present, no coincidence of centers of positive and negative charge); and
- by the so-called electrophoretic effect (enhancement of viscous drag due to movement of central ion in opposite direction of ionic atmosphere);

(see, e.g., [54,55]), with[9]

$$\frac{\Lambda_m}{\nu_\pm z_\pm} = \frac{\Lambda_m^0}{\nu_\pm z_\pm} - \bar{\kappa}\left(A\frac{\Lambda_m^0}{\nu_\pm z_\pm} + B\right)\sqrt{c} \tag{17}$$

with $\nu_\pm z_\pm = \nu_+ z_+ = \nu_- z_-$ and

$$\bar{\kappa} = \left(\frac{e^2 N}{\epsilon k T}\right)^{1/2}\left(\nu_+ z_+^2 + \nu_- z_-^2\right)^{1/2},\quad A = \frac{z_+ z_- e^2}{24\pi\epsilon k T}\frac{2q}{1+\sqrt{q}},\quad \text{and}\quad B = \frac{Ne^2(z_+ + z_-)}{6\pi\eta}. \tag{18}$$

In Eq. (17), $\bar{\kappa}A$ and $\bar{\kappa}B$ consider the relaxation and the electrophoretic effect, respectively. In Eq. (18), $N$ is the Avogadro number, $k$ is the Boltzmann constant (see Table B.5 in Appendix B), $T$ is the temperature in [K], and $\epsilon$ [C$^2$/(J m)] the electric permittivity of water. The latter shows a temperature dependency as

$$\epsilon(T) = \epsilon_0 \epsilon_{rel}(T), \tag{19}$$

[7] For Portlandite $Ca(OH)_2$, the molar concentration of the electrolyte is equal to the concentration of the cation $Ca^{2+}$, as the number of cations per stoichiometric unit of the electrolyte is one.

[8] The viscosity $\eta$ shows a pronounced temperature dependency (decreasing with increasing temperature) characterized by [53]

$$\eta = 1.002 \times 10^{-3} \times 10^{-A/B} \text{ in [Pa s]}\quad \text{with } A = 1.37023(T-20) + 8.36 \times 10^{-4}(T-20)^2 \text{ in [°C]}\quad \text{and } B = 109 + T \text{ in [°C]}, \tag{15}$$

giving $\eta(T = 25\,°C) = 0.89 \times 10^{-3}$ Pa s.

[9] In standard text books, $\Lambda_m/(\nu_\pm z_\pm)$ and $\Lambda_m^0/(\nu_\pm z_\pm)$ are denoted as "equivalent" and "limiting equivalent" conductivity, respectively (see, e.g., [55]).

**Table 1**
Number of cations and anions per stoichiometric unit, number of elementary charges of cation and anion, ionic mobilities at $T=298$ K, conductivities of ions at $T=298$ K for investigated electrolytes [53].

| Electrolyte | $\nu_+$ | $\nu_-$ | $z_+$ | $z_-$ | $u_+$ | $u_-$ | $\lambda_+^0$ | $\lambda_-^0$ |
|---|---|---|---|---|---|---|---|---|
| | [−] | [−] | [−] | [−] | [$10^{-8}$ m$^2$/(sV)] | | [$10^{-3}$Sm$^2$/mol] | |
| $NaOH \rightarrow Na^+ + OH^-$ | 1 | 1 | 1 | 1 | 5.19 | 20.64 | 5.01 | 19.91 |
| $KOH \rightarrow K^+ + OH^-$ | 1 | 1 | 1 | 1 | 7.62 | 20.64 | 7.35 | 19.91 |
| $NaCl \rightarrow Na^+ + Cl^-$ | 1 | 1 | 1 | 1 | 5.19 | 7.91 | 5.01 | 7.63 |
| $CuSO_4 \rightarrow Cu^{2+} + SO_4^{2-}$ | 1 | 1 | 2 | 2 | 5.56 | 8.29 | 10.72 | 16.00 |
| $CaCl_2 \rightarrow Ca^{2+} + 2Cl^-$ | 1 | 2 | 2 | 1 | 6.17 | 7.91 | 11.90 | 7.63 |
| $Ca(OH)_2 \rightarrow Ca^{2+} + 2OH^-$ | 1 | 2 | 2 | 1 | 6.17 | 20.64 | 11.90 | 19.91 |

where $\epsilon_0$ is the vacuum permittivity (see Table B.5 in Appendix B) and the relative permittivity $\epsilon_{rel}(T)$ is given for different temperatures in Table B.6 (see Appendix B). Finally, $q$ is a constant dependent on the symmetry ($z_+ = z_-$) or asymmetry ($z_+ \neq z_-s$) of the electrolyte with [54,55]

$$q = \frac{z_+ z_-}{z_+ + z_-} \frac{\lambda_+^0 + \lambda_-^0}{z_+ \lambda_-^0 + z_- \lambda_+^0}. \tag{20}$$

Fig. 4(a) and (b) shows a comparison between test results (symbols) and model prediction (solid lines) for some symmetrical and asymmetrical electrolyte solutions. Hereby, test data for KOH and NaOH was taken from [56], test data for $CuSO_4$ and $Ca(OH)_2$ from [57]. In order to highlight the pronounced temperature influence on the molar conductivity, the model prediction for temperatures ranging from 10 to 30 °C is shown for NaCl and $Ca(OH)_2$.

*2.4.1. Estimation of $D_{sol}$ from molar conductivity*

For the borderline case of the molar concentration approaching zero, Einstein's relation gives access to the diffusion coefficient of the cations/anions as [53]

$$D_\pm^0 = \frac{u_\pm RT}{z_\pm F} = \frac{\lambda_\pm^0}{z_\pm F} \frac{RT}{z_\pm F}. \tag{21}$$

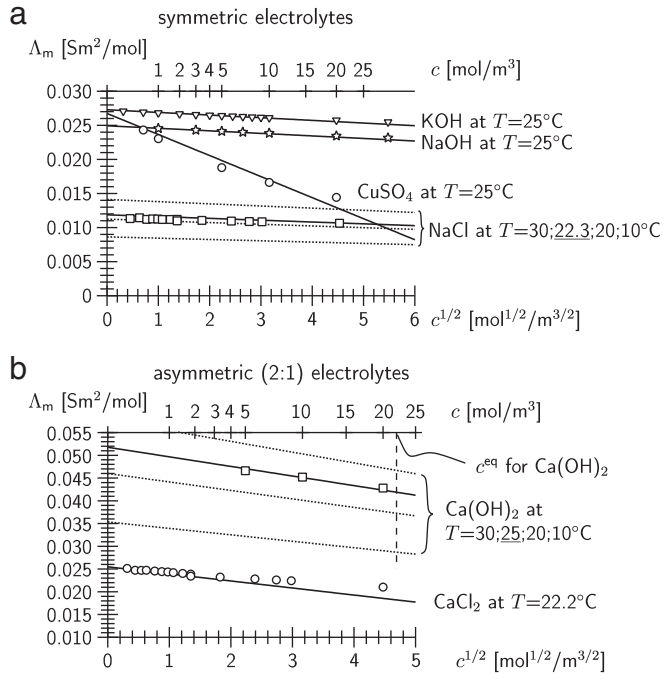


**Fig. 4.** Molar conductivities of (a) symmetrical and (b) asymmetrical aqueous electrolyte solutions.

For $Ca(OH)_2$ (at $T=298$ K, see Table 1), the diffusion coefficient of the cation $Ca^{2+}$ and the anion $OH^-$ becomes $D_+^0 = 7.9\times10^{-10}$ m$^2$/s and $D_-^0 = 53\times10^{-10}$ m$^2$/s, respectively. The diffusion potential created by the different diffusion coefficients of cations and anions speeds up the cations while it slows down the anions and the electrolyte diffusion coefficient is given as [58,27]

$$D_{sol}^0 = \frac{D_+^0 D_-^0 (z_+ + z_-)}{z_+ D_+^0 + z_- D_-^0} \tag{22}$$

and amounts to $18.2\times10^{-10}$ m$^2$/s for $Ca(OH)_2$ (at $T=298$ K).

In order to estimate the diffusion coefficient for higher molar concentrations, $D_{sol} = D_{sol}(c)$, a function describing the concentration dependency, $\alpha(c)$, is introduced based on the molar conductivity of the electrolyte solution (Eq. (17)):

$$\Lambda_m(c) = \alpha(c)\Lambda_m^0 \;\rightarrow\; \alpha(c) = 1 - \overline{\kappa}\left(A + B\frac{\nu_\pm z_\pm}{\Lambda_m^0}\right)\sqrt{c}. \tag{23}$$

Assuming that the molar conductivity of the electrolyte solution for higher molar concentrations, $\Lambda_m$, can be written in the same form as the limiting molar conductivity of the electrolyte solution, $\Lambda_m^0$, (see Eq. (13)) gives

$$\text{assumption (i)} : \Lambda_m(c) = \nu_+\lambda_+(c) + \nu_-\lambda_-(c). \tag{24}$$

Multiplying Eq. (13) by $\alpha(c)$ gives

$$\alpha(c)\Lambda_m^0 = \Lambda_m(c) = \alpha(c)\nu_+\lambda_+^0 + \alpha(c)\nu_-\lambda_-^0. \tag{25}$$

The right hand sides of Eqs. (24) and (25) coincide if

$$\lambda_\pm(c) = \alpha(c)\lambda_\pm^0. \tag{26}$$

Here, we further underlie that the concentration dependent diffusion coefficient of cations/anions and of the electrolyte solution (compare to Eqs. (21) and (22)) can be written as

$$\text{assumption (ii)} : D_\pm(c) = \frac{\lambda_\pm(c)}{z_\pm F}\frac{RT}{z_\pm F}. \tag{27}$$

and

$$\text{assumption (iii)} : D_{sol}(c) = \frac{D_+(c)D_-(c)(z_+ + z_-)}{z_+ D_+(c) + z_- D_-(c)}. \tag{28}$$

Hence, inserting Eq. (26) into Eq. (27) gives

$$D_\pm(c) = \frac{\alpha(c)\lambda_\pm^0}{z_\pm F}\frac{RT}{z_\pm F}, = \alpha(c)D_\pm^0 \tag{29}$$

and the concentration dependent diffusion coefficient of the electrolyte solution can be written as

$$D_{sol}(c) = \frac{\alpha(c)D_+^0\alpha(c)D_-^0(z_+ + z_-)}{z_+\alpha(c)D_+^0 + z_-\alpha(c)D_-^0} = \alpha(c)D_{sol}^0. \quad (30)$$

Fig. 5(a) shows a comparison between test data for NaCl and $CaCl_2$ [55] (symbols) and the estimation based on Eq. (30) (solid lines), showing good agreement especially for $c<\sim 1$ mol/m$^3$. Fig. 5(b) depicts the temperature dependency of $D_{sol}(c)$ for $Ca(OH)_2$. The average value (e.g. for $c=0.5c^{eq}$ at $T=20$ °C) of $13.5\times10^{-10}$ m$^2$/s is, however, approximately an order of magnitude larger than $D_{sol}$ determined by backcalculation of leaching experiments on cement paste in deionized water based on the differential scheme (see Section 2). Hence, the rather low value for $D_{sol}$ cannot solely be explained by its concentration dependency (see Fig. 5(b)), as suggested previously in the open literature (see, e.g., [20]).

### 2.5. Subsequent leaching/decalcification

As already stated in the Introduction, for leaching in deionized water,

1. portlandite CH;
2. hydration products from $C_3A$ and $C_4AF$ hydration: ettringite ($C_6A\bar{S}_3H_{32}$), monosulfate ($C_4A\bar{S}H_{12}$), $C_4AH_{13}$, and hydrogarnet ($C_3(A,F)H_6$); and
3. C–S–H

are considered to be dissolved/decalcified subsequently from the solid skeleton.

By conducting leaching experiments on cement paste and mortar in 6 molar (6 M) ammonium nitrate ($NH_4NO_3$) solution, the duration of experiments can be reduced significantly, with leaching rates two orders of magnitude larger than leaching rates in deionized water.

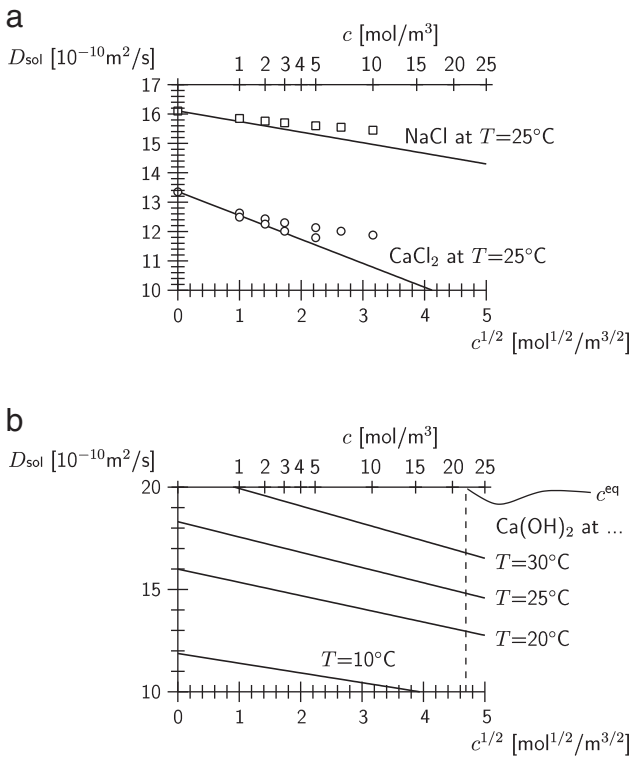


**Fig. 5.** Electrolyte diffusion coefficient $D_{sol}$ for (a) NaCl and $CaCl_2$ (test data taken from [55]) and (b) $Ca(OH)_2$ at different temperatures.

The equilibrium calcium concentration of a solution saturated in CH increases from 0.022 mol/l in water to 2.9 mol/l in a 6 M $NH_4NO_3$ solution [2] (respective values given in [12]: from 0.021 mol/l to 2.73 mol/l); the characteristics of leaching in 6 M $NH_4NO_3$ solution may be summarized as:

- the effects of $NH_4NO_3$ leaching on the microstructure of cement paste are similar to the effects of water leaching; however, there are differences in the progressed state of leaching, i.e., when the Ca/Si or C/S molar ratio of the decalcified solid drops below 1;
- recent research on the solubility on white Portland cement paste [59] indicates that the part of Ca bound in sulfoaluminate phases (ettringite, monosulfate, ...) is relatively insoluble in 6 M $NH_4NO_3$ solution (see dissolution experiments on white Portland cement paste at Ca/Si molar ratios <1 in [59]); according to [60], ettringite is not dissolved.

Hence, for leaching in 6 M $NH_4NO_3$ solution

1. portlandite CH and
2. C–S–H

are considered to be dissolved/decalcified subsequently from the solid skeleton. Hydration products from $C_3A$ and $C_4AF$ hydration are considered as insoluble in the analyzes.

## 3. Re-analysis of leaching experiments

The field equation for calcium dissolution and diffusion reads for material isotropy [12]:

$$\frac{\partial}{\partial t}(\phi c) + \frac{\partial}{\partial t}s = c\dot{\phi} + \phi\dot{c} + \dot{s} = -\nabla\cdot\mathbf{q} = \nabla\cdot(D_{eff}\mathbf{I}\cdot\nabla c), \quad (31)$$

with $\mathbf{q}$ [mol/(dm$^2$h)] as the molar flux linked to the concentration gradient in the pore solution by Fick's law. In Eq. (31), porosity $\phi$ and solid calcium concentration $s$ are functions of the calcium concentration in the pore solution, $\phi=\phi(c)$ and $s=s(c)$, respectively. For the re-analysis of leaching experiments, field Eq. (31) is solved by means of the finite-element method (FEM), see Appendix A.

These leaching experiments were characterized by placing either disc-, plate-, or cylinder-shaped specimens (age > 2 month) in a reservoir containing the aggressive solution (deionized water or 6-molar ammonium-nitrate (6 M $NH_4NO_3$) solution). While the calcium concentration in the reservoir was recorded at discrete time instants, the reservoir was continuously stirred in order to prevent a concentration gradient within the reservoir. Fig. 6 shows the employed 1D and axisymmetric models for the respective specimens, characterized by the partial sealing by epoxy (circumference of disc- or plate-shaped specimens, bottom and top of cylinder-shaped specimens).

### 3.1. Leaching experiments on white cement paste specimens

The mass fractions of the main clinker phases in the employed white cement were determined by Rietveld analysis of XRD data (see Table 2). In a differential thermal analysis, the CH content of the hydrated cement paste used for the leaching experiments with a $w/c=0.53$ was determined as $m_{CH}=21.3$ m-% for dried samples. Using the molar weights of CH, with $\mathcal{M}_{CH}=74$ g/mol and a (dried) paste density[10] of $\rho=1653$ g/dm$^3$, the calcium concentration in the solid attributed to CH amounts to $s_{CH}^0 = m_{CH}/\mathcal{M}_{CH}\times\rho = 0.213/74\times1653 = 4.8$ mol/dm$^3$. This compares well to the value predicted by the hydration stoichiometry model (see Eqs. (1) to (6)) of $s_{CH}^0 = 4.7$ mol/dm$^3$. Other key values predicted by the stoichiometry model relevant for leaching analyzes are: total amount of calcium bound in

[10] Unit weight from hydration stoichiometry model = 1797 g/dm$^3$; saturated capillary pore space = 14.4%, giving $\rho = 1797 - 0.144\times998 = 1653$ g/dm$^3$.

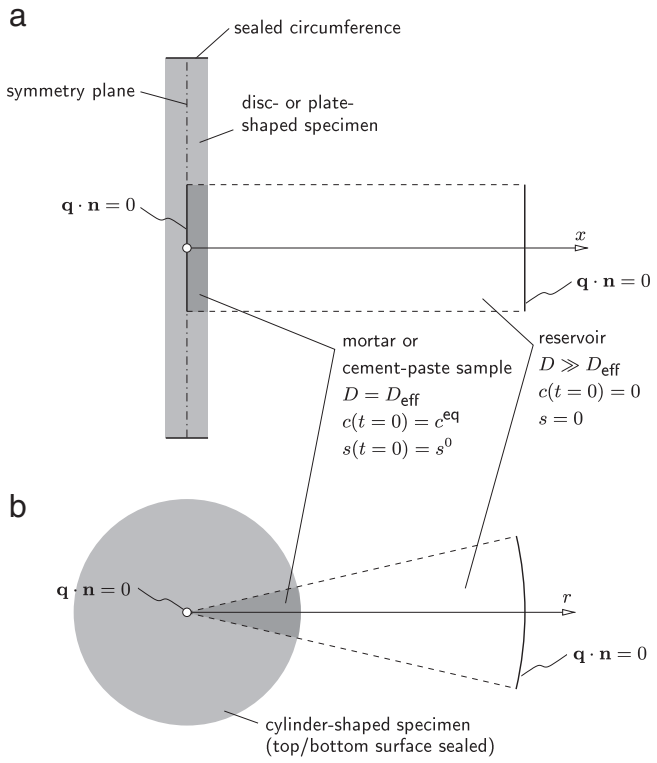


**Fig. 6.** (a) 1D and (b) axisymmetric model for re-analysis of leaching tests on disc- and plate-shaped and cylinder-shaped specimens, respectively.

the solid skeleton $s^0 = 13.9$ mol/dm$^3$, $s^0_{C-S-H} = 7.8$ mol/dm$^3$, initial capillary pore space $\phi_{cap} = 20.1\%$, $\phi^{max}_{CH} = 15.5\%$, $\phi^{max}_{C-S-H} = 31.4\%$ (using a maximum phase porosity $\bar{\phi}^{max}_{C-S-H}$ of 0.6, see Section 2.3). For the re-analysis of leaching experiments, two different modes of sequential CH dissolution/C–S–H decalcification are considered (see Fig. 7):

1. CH dissolution within $0.95 \le c/c^{eq} \le 1$ ("fast CH dissolution"), C–S–H decalcification within $0 \le c/c^{eq} < 0.95$;
2. CH dissolution within $0.65 \le c/c^{eq} \le 1$ ("slow CH dissolution"), C–S–H decalcification within $0 \le c/c^{eq} < 0.65$.

Based on $D_{sol} = 2.5 \times 10^{-10}$ m$^2$/s, the evolution of calcium concentration in the sample enclosing reservoir from the leaching test is represented satisfactorily (see Fig. 8). Only the first few measurements are overestimated by the analysis. For these rather small time instants the data is, however, characterized by a slope in the double-logarithmic diagram greater than 1/2.

### 3.2. Leaching experiments on ordinary Portland cement paste and mortar specimens

The ordinary Portland cement (OPC) employed for sample preparation was already characterized by a CH content of 2.8 m-% and a free lime content of 1.5 m-% (see Table 3). For paste with $w/c = 0.50$ this amounts[11] to a Ca-content of $s^0_{CH,init} = 0.8$ mol/dm$^3$. This result together with the hydration stoichiometry model gives $s^0 = s^0_{CH,init} + s^0_{hyd} = 0.8 + 13.7 = 14.5$ mol/dm$^3$, $s^0_{CH} = s^0_{CH,init} + s^0_{CH,hyd} = 0.8 + 4.1 = 4.9$ mol/dm$^3$, $s^0_{C-S-H} = 7.2$ mol/dm$^3$, initial capillary pore space $\phi_{cap} = 19.6\%$, $\phi^{max}_{CH} = 2.6 + 13.7 = 16.3\%$, $\phi^{max}_{C-S-H} = 29.0\%$ (using $\bar{\phi}^{max}_{C-S-H}$ of 0.6).

In a differential thermal analysis the CH content of the hydrated cement paste was determined as 19.8 m-%. Employing a paste unit weight (dried)[12] of $\rho = 1712$ g/dm$^3$, the calcium concentration in the solid attributed to CH amounts to $s^0_{CH} = m_{CH}/\mathcal{M}_{CH} \times \rho = 0.1982/74 \times 1712 = 4.6$ mol/dm$^3$ comparing well to the value of 4.9 mol/dm$^3$ predicted by the hydration stoichiometry model.

The linear material functions employed for accelerated leaching experiments on paste specimens with $w/c = 0.50$ are given in Fig. 9. On the other hand, leaching experiments were conducted on mortar specimens characterized by mix proportion of 225 g water, 450 g cement, and 1350 g quartz sand, hence $w/c = 0.50$ and a volume fraction of cement paste in the material system of 0.42.[13] Thus, for re-analysis of accelerated leaching experiments, the material functions for mortar correspond to the material functions for paste (with the same $w/c = 0.50$) scaled by a factor of 0.42 (see Fig. 9). Employing $D_{sol} = 2.5 \times 10^{-10}$ m$^2$/s, as identified by the accelerated leaching experiments on white cement paste specimens, both accelerated leaching experiments on OPC paste (Fig. 10(a)) and mortar (Fig. 10(b)) were re-analyzed showing good agreement with the test data.

Besides the accelerated leaching experiments, a disc-shaped OPC paste specimen characterized by $w/c = 0.5$ was leached in deionized water (see Fig. 11). For backcalculation of test data, polylinear equilibrium functions for $s = s(c/c^{eq})$ and $\phi = \phi(c/c^{eq})$ (see Fig. 12) were considered, with the location of the kinks along the $c/c^{eq}$ axis set according to the data given in Fig. 1(b) [33] at $c = 0.001$; 0.002; 0.018; 0.020 mol/l, i.e., at $c/c^{eq} = 0.045$; 0.091; 0.818; 0.909 with $c^{eq} = 0.022$ mol/l (see Fig. 12). The values for $s^0$, $s^0_{CH}$, $s^0_{C-S-H}$, … $\phi_{cap}$, $\phi^{max}_{CH}$, $\phi^{max}_{C-S-H}$, defining the location of the kinks of the aforementioned polylinear functions $s = s(c/c^{eq})$ and $\phi = \phi(c/c^{eq})$ along the $s$ and $\phi$ axis, respectively, were determined from the hydration stoichiometry model. Hereby, the amount of calcium bound in sulfoaluminates and hydrogarnet amounts to 2.4 mol/dm$^3$. Akin to decalcification of CSH, the phase porosity of sulfoaluminates and hydrogarnet after complete decalcification was set to $\bar{\phi}_x = 0.6$. The other key values needed for defining the equilibrium curves have already been listed previously in the context of the material function employed for the accelerated tests. In accordance with [4] CH, monosulfate, ettringite, and CSH are dissolved or decalcified subsequently during leaching (see Fig. 12).

When using a value for $D_{sol}$ describing diffusive transport in bulk water ($D_{sol} = 10 \times 10^{-10}$ m$^2$/s), the evolution of the calcium concentration in the reservoir is crudely overestimated (see Fig. 11). A possible explanation, already reasoned for NaCl diffusion, is so-called structuring of water in charged porous media including bentonite clays [61] and cement-based materials [27]. For the latter, the diffusion coefficient in the pore fluid and the one in bulk solution ($D_{sol} \sim 16 \times 10^{-10}$ m$^2$/s, see Fig. 5(a)) differs by the factor 15. Structuring of water refers to layering of water molecules along charged surfaces, e.g., in clay–water–NaCl systems [61] resulting in an increase of viscosity $\eta$ of near-surface water. Molecular dynamics calculations reported in [61] give a thickness of

**Table 2**
Rietveld analysis of white Portland cement.

| Phase | Mass fraction $m_x$ [m-%] |
|---|---|
| $C_3S$ | 66.2 |
| $C_2S$ | 17.2 |
| $C_3A$ | 6.4 |
| $C_4AF$ | 2.0 |
| Gypsum | 1.0 |
| Halfhydrate | 3.2 |
| Anhydrite | 0.3 |
| Dolomite $CaMg(CO_3)_2$ | 3.9 |
| Calcite $CaCO_3$ | 0.3 |

[11] Molar weight of Ca = 40 g/mol, molar weight of free lime = 56 g/mol, molar weight of CH = 74 g/mol; Ca-content in cement from CH and free lime of $2.8 \times 40/74 + 1.5 \times 40/56 = 1.51 + 1.07 = 2.59$ m-%; cement mass in 1 dm$^3$ cement paste (with $w/c = 0.5$) = $1000/(1000/3150 + 500/998) = 1222$ g/dm$^3$; Ca mass content = $2.59/100 \times 1222 = 31.6$ g/dm$^3$; Ca molar fraction = $31.6/40 = 0.8$ mol/dm$^3$.

[12] Unit weight from hydration stoichiometry model = 1838 g/dm$^3$; saturated capillary pore space = 12.65%, giving $\rho = 1838 - 0.1265 \times 998 = 1712$ g/dm$^3$.

[13] resulting material volume of mortar employing unit weights of water, cement, and quartz sand of 998, 3150, and 2650 g/dm$^3$: $225/998 + 450/3150 + 1350/2650 = 0.878$ dm$^3$ giving the volume fraction of cement paste: $(225/998 + 450/3150)/0.878 = 0.42$.

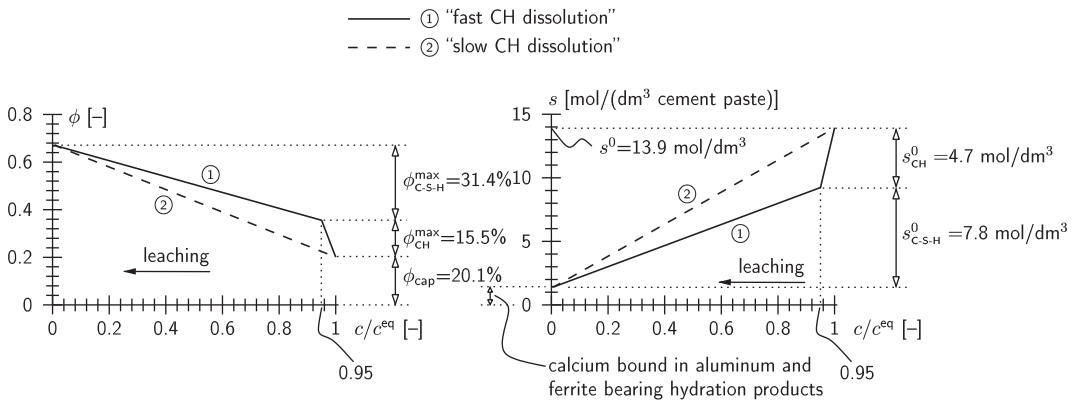


**Fig. 7.** Material functions employed for analysis of accelerated leaching experiment on white cement paste specimens, $c^{eq}=2.9$ mol/l.

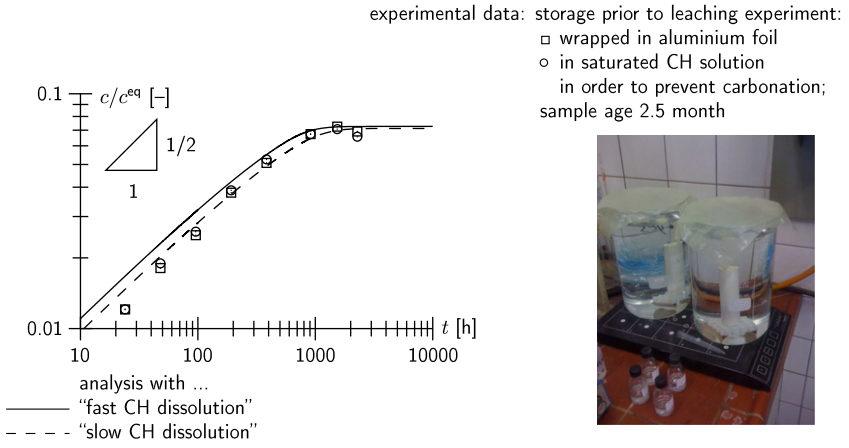


**Fig. 8.** Re-analysis of accelerated leaching test on white cement paste cylinders (diameter 28.8 mm, length 130 mm, surface in contact with the aggressive solution $28.8\,\pi 130 = 11{,}762$ mm$^2$): evolution of calcium concentration in reservoir (5000 ml 6 M $NH_4NO_3$ solution, $c^{eq}=2.9$ mol/l).

the structurally ordered water layer in contact with the surface of approximately 0.5 nm for pure water (see Fig. 2 and its discussion in [61]). According to [61], viscosity and diffusion coefficient change rapidly in a 3–4 nm thick layer, with the viscosity $\eta$ decreasing from ~15 Pa s toward its value in bulk condition of ~1 Pa s and diffusion coefficient increasing from zero to its value in bulk solution (see Fig. 2 in [61]).

The ionic mobility is inversely proportional to $\eta$ (see Eq. (16)), $D^0_{\pm}$ and consequently $D^0_{sol}$ will decrease by the same factor by which $\eta$ increases.[14] In [62], the internal surface of white cement paste with $w/c=0.5$ was determined by small angle neutron scattering (SANS) and nitrogen BET (Brunauer Emmett Teller gas adsorption theory) at different leaching states (leaching in ammonium-nitrate solution). Hereby, the internal surface area increased from $\sim 1.1\times10^8$ m$^2$/m$^3$ (SANS for unleached state, Ca/Si-ratio = 3, value for BET: $0.8\times10^8$ m$^2$/m$^3$) to $\sim 1.8\times10^8$ m$^2$/m$^3$ (SANS for leached state with Ca/Si-ratio = 1, value for BET: $1\times10^8$ m$^2$/m$^3$). Underlying a mean value for the internal surface area of $1.2\times10^8$ m$^2$/m$^3$ (see Fig. 9 in [62]) and a thickness of the layer influenced by structuring of $3\text{ nm}=3\times10^{-9}$ m, the volume fraction of the latter amounts to 0.36 m$^3$/m$^3$ = 36%. Hence, a fair amount of the pore liquid in cement-based materials may be characterized as influenced by structuring with increased viscosity and, hence, decreased diffusivity.

When employing $D_{sol}=0.3\times10^{-10}$ m$^2$/s in the analysis (see Fig. 11), justified by the decreased diffusivity in the case of layered pore water with increased viscosity, the test data is represented well with an initial slope in the double-logarithmic diagram of 1/2. Only for small time instants (i.e., at $t=2$, 4, 8 h), the numerical result exceeds the experimental result. This behavior can be explained by a dissolution kinetics law recently proposed by [34], with the characteristic time of leaching denoted as $\tau$ (for the algorithmic treatment within the underlying finite-element formulation see Appendix B). Hereby the equilibrium curves in Fig. 12 characterize the limiting dissolution state, hence, they are not reached immediately (as assumed until now) upon a decrease of $c$ in the pore liquid. When employing the dissolution kinetics law with a characteristic time $\tau$ of 200 h, the test data for small time instants is represented better, while for larger times the result coincides with the re-analysis underlying instantaneous dissolution. Note, that the used value of $\tau$ is about two orders of magnitude larger than the values given in [34], with e.g. $\tau=3.25$ h. The latter value was, however, estimated based on the diffusion coefficient representing transport in bulk water with $D_{sol}\sim10\times10^{-10}$ m$^2$/s, what is in turn two orders of magnitude larger

**Table 3**
Rietveld analysis of ordinary Portland cement.

| Phase | Mass fraction $m_x$ [m-%] |
|---|---|
| Alite $C_3S$ monoclinic | 64.7 |
| Belite $C_2S$ | 10.65 |
| $C_3A$ cubic | 2.0 |
| $C_4AF$ Brownmillerite | 11.8 |
| Bassanite $2CaSO_4{\cdot}H_2O$ | 1.4 |
| Anhydrite | 3.8 |
| Free lime CaO | 1.5 |
| $CaCO_3$ | 0.3 |
| Periclase MgO | 0.9 |
| Portlandite | 2.8 |
| Quartz | 0.1 |

[14] See molecular dynamics calculations in [61], where an increase of $\eta=0.001$ Pa s to 0.007 Pa s results in a decrease of $D_{sol}$ from $17\times10^{-10}$ m$^2$/s to $2.5\times10^{-10}$ m$^2$/s, i.e., $0.007/0.001=(2.5/17)^{-1}=7$.

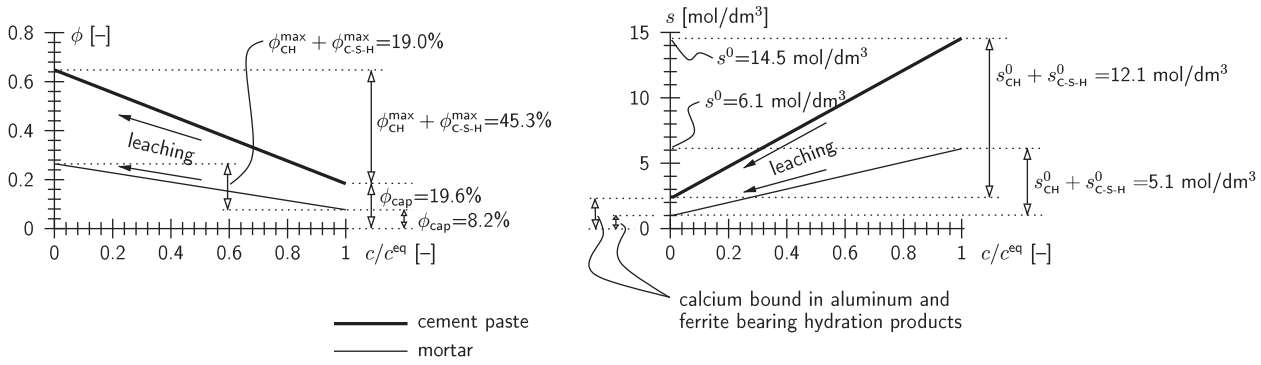


**Fig. 9.** Linear material functions employed for analysis of accelerated leaching experiment on ordinary Portland cement paste/mortar specimens, $c^{eq}=2.9$ mol/l.

than the diffusion coefficient employed in the present analysis with $D_{sol}=0.3\times10^{-10}$ m$^2$/s, accounting for layers of structured water in the pore structure of cement-based materials.

In order to experimentally validate the material function $\phi(c)$, the porosity of (i) sound cement paste and (ii) completely leached cement paste (6 M $NH_4NO_3$ leaching) was determined by water saturation under vacuum and oven drying at 105 °C (see [3] for outline of experimental method). Two successive wetting–drying cycles were performed, i.e., wetting–drying–wetting–drying, with C–S–H-LD expected to transform into its stable form [63] after the first drying. For sound cement paste, the density decrease between the saturated and oven-dried states amounts to $\Delta\rho_{exp}=0.391$ g/cm$^3$ in the second wetting–drying cycle (in first cycle: $\Delta\rho_{exp}=0.406$ g/cm$^3$). Scaling by the density of water $\rho_H=1$ g/cm$^3$ gives access to the porosity with contributions from the capillary porosity $\phi_{cap}$ and the release of gel water in C–S–H and of crystal water from ettringite and monosulfate:

$$\frac{\Delta\rho_{exp}}{\rho_H}=\phi_{cap}+\frac{\Delta\rho_{C-S-H}}{\rho_H}f_{C-S-H}+0.529f_{ett}+0.338f_{mono}. \quad (32)$$

Hereby, the porosity induced by ettringite dehydration was estimated based on the molar volumes given in [40] for the saturated state of

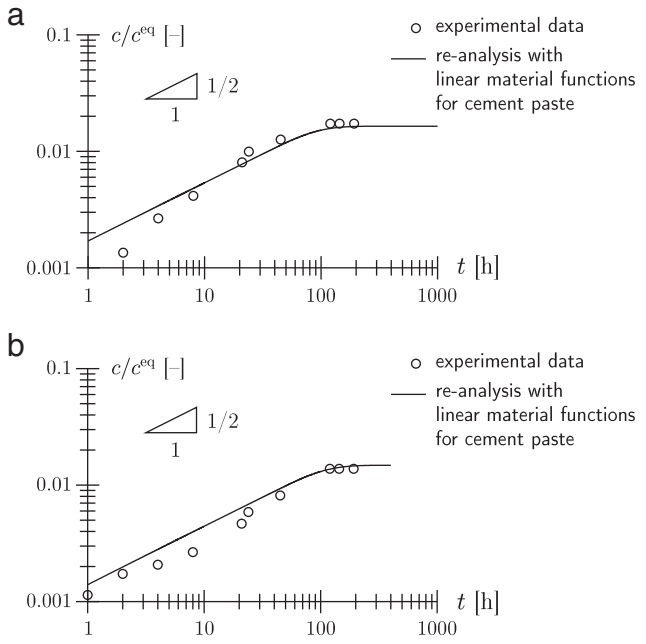


**Fig. 10.** Re-analysis of accelerated leaching tests, evolution of calcium concentration in reservoir (1000 ml 6 M $NH_4NO_3$ solution, $c^{eq}=2.9$ mol/l): (a) ordinary Portland cement paste disc (diameter 29.0 mm, thickness 5.8 mm, surface in contact with the aggressive solution $2\times29.0^2\pi/4=1321$ mm$^2$) and (b) ordinary Portland cement mortar plate ($39.9\times40.4\times5.07$ mm, surface in contact with the aggressive solution $2\times39.9\times40.4=3224$ mm$^2$).

717 cm$^3$/mol and for the dried state of 338 cm$^3$/mol as 1–338/717 = 0.529 (for monosulfate 1–229/346 = 0.338). The density decrease of C–S–H gel due to drying was determined as 0.30 g/cm$^3$ for C–S–H-HD and 0.35 g/cm$^3$ for stable C–S–H-LD (see Table 4 in [63] and [45]). Considering volume fractions of C–S–H-LD and C–S–H-HD in C–S–H as 0.7 and 0.3 [50,40], respectively, appropriate for $w/c=0.5$, the density decrease of C–S–H is estimated as $\Delta\rho_{C-S-H}=0.7\times0.35+0.3\times0.30=0.335$ g/cm$^3$. With volume fractions of C–S–H, ettringite, and monosulfate of $f_{C-S-H}=0.483$, $f_{ett}=0.064$, and $f_{mono}=0$ obtained from the hydration kinetics model, Eq. (32) gives a value for the capillary porosity $\phi_{cap}$ of the sound material of $0.391-0.335\times0.483-0.529\times0.064=0.195$ compared to the value used in the numerical analysis of 0.196 (see Figs. 9 and 12), derived from the hydration kinetics model solely.

For completely leached cement paste (6 M $NH_4NO_3$ leaching), the density decrease between saturated and oven-dried state was determined experimentally as $\Delta\rho_{exp}=0.744$ g/cm$^3$ in the second wetting–drying cycle (in first cycle: $\Delta\rho_{exp}=0.777$ g/cm$^3$). Since – to the authors' knowledge – no studies on the density decrease due to drying of decalcified C–S–H gel are available, the same density decrease as for sound C–S–H gel of 0.335 g/cm$^3$ is assumed. The volume fraction of decalcified C–S–H is reduced to $f_{C-S-H}=(1-0.6)\times0.483=0.193$, accounting for $\bar{\phi}_{C-S-H}^{max}=0.6$ as determined in Section 3. Finally, Eq. (32) gives $\phi(c/c^{eq}=0)=0.744-0.335\times0.193-0.529\times0.064=0.645$ as compared to 0.649 used in the numerical analyzes, derived from the hydration kinetics model solely (see Fig. 9(a), $\phi(c/c^{eq}=0)$ for cement paste).

## 4. Summary and outlook

In this paper, a differential-scheme based formulation for diffusive transport of calcium in the (micro)porous space of cement-based materials, accounting for the actual material composition with regards to the calcium content bound in the solid skeleton and the increase of porous space due to calcium leaching, was presented. Considering this material model within an axisymmetric finite element formulation, leaching tests on cement paste and mortar were re-analyzed. Hereby, the formulation based on non-periodic homogenization methods constitutes a sound description of changing material composition and morphology in the course of material degradation due to calcium leaching. In addition to (i) the micro-to-macro transition of diffusive transport properties established by the differential scheme, (ii) the equilibrium function relating calcium concentration bound in the solid material skeleton to the calcium concentration in the pore fluid $s(c)$, and (iii) the diffusion coefficient characterizing the interstitial pore fluid, $D_{sol}$, constitute key quantities for the analysis.

Whereas $s(c)$ is well established and generally agreed upon in the open literature, $D_{sol}$ in bulk aqueous solution was estimated based on standard physical chemistry arguments. The re-analysis of leaching tests, however, revealed that $D_{sol}$ characterizing the interstitial pore

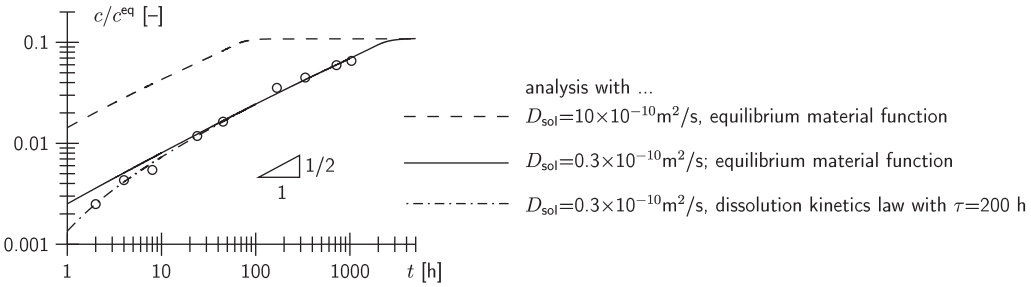


**Fig. 11.** Re-analysis of leaching test (deionized water) on ordinary Portland cement paste disc (diameter 28.9 mm, thickness 1.15 mm, surface in contact with the aggressive solution $2\times28.9^2\pi/4=1312$ mm$^2$): evolution of calcium concentration in reservoir (2290 ml deionized water, $c^{eq}=0.022$ mol/l); a medium (smeared) degradation depth can be determined as [depth in mm] = [concentration in reservoir in mol/l] × [reservoir volume in l]/[sample surface in mm$^2$]/[initial calcium concentration bound in solid skeleton $s^0$ in mol/mm$^3$].

fluid in cement paste is by a factor of ~1/45 smaller than $D_{sol}$ of aqueous solutions. A similar reduction was observed for chloride diffusion in the pore systems of cement-based materials and may be explained by the increased viscosity of water due to layers of so-called structured water along the charged internal surface of cement-based materials.

For re-analysis of the initial part of leaching experiments, characterized by a rapid drop in the interstitial calcium concentration, the use of the kinetics law proposed in [18,34] has proved beneficial. Hereby, the equilibrium functions $s(c)$ and $\phi(c)$ represent the limiting dissolution state.

Future work will focus on the extension of the described dissolution/diffusion model towards the prediction of mechanical performance after leaching with a multiscale representation of the porous space, i.e., separation in two or several species. As pointed out in [3], the substantial stiffness and strength degradation is accompanied by an increase of pore pressure sensitivity. In the scopes of a description as a poroelastic material, the (macroscopic) Biot's coefficient is expected to rise with the increase of the capillary porosity due to CH leaching. On the other hand, decalcification of C–S–H alters Biot's coefficient at the smallest scale of observation, making the material extremely pressure sensitive [3,2].

## Acknowledgments

Financial support by the Austrian Research Promotion Agency Ltd. (FFG) for project "Numerical simulation of leaching behavior of cement-based materials for underground construction" (project number 824908) is gratefully acknowledged. The authors thank Markus Astner and Saskia Bernstein (Geosystem Spezialbaustoffe GmbH, Rohrdorf, Germany) and Franz Kritzinger (Zementwerk Hatschek GmbH, Gmunden, Austria) for fruitful discussions and helpful comments within this research project.

## Appendix A. Algorithmization in the scope of axisymmetric FE formulation

The field equation for the axisymmetric dissolution/diffusion problem (with radial coordinate $r$) is given by

$$\frac{\partial q}{\partial r}+\frac{q}{r}+\frac{\partial \phi}{\partial t}c+\phi\frac{\partial c}{\partial t}+\frac{\partial s}{\partial t}=0, \tag{A.1}$$

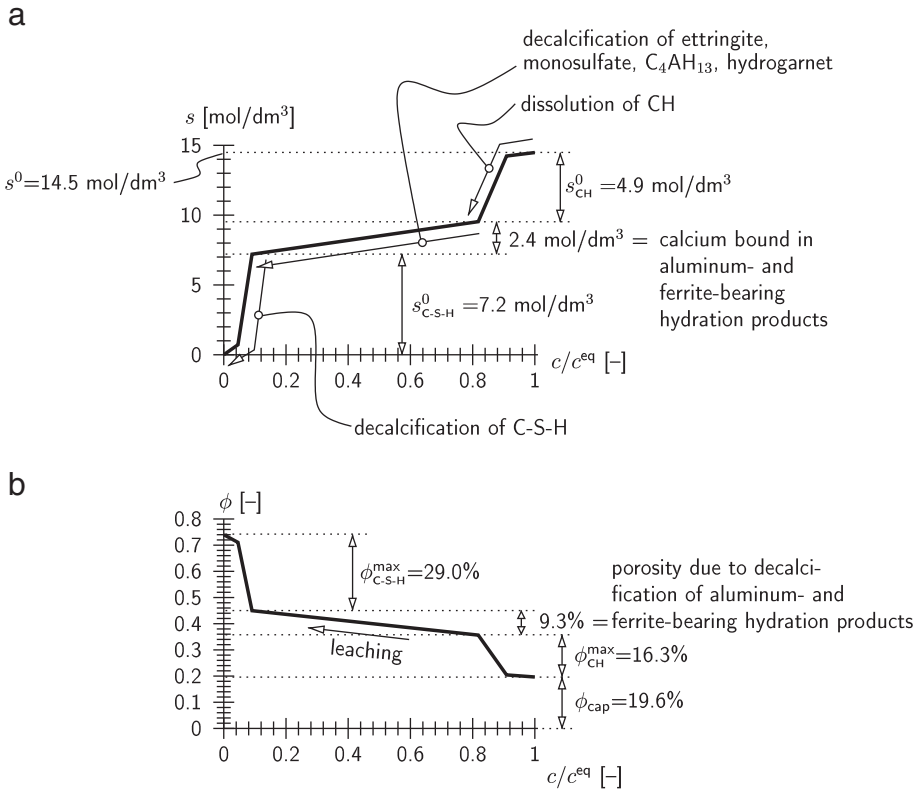


**Fig. 12.** Material functions employed for analysis of leaching experiment (deionized water) on ordinary Portland cement paste specimens, $c^{eq}=0.022$ mol/l.

where $q$ is the ionic flux. Inserting Ficks's law specialized for axisymmetric conditions, $q=-D_{\text{eff}}\partial c/\partial r$ into Eq. (A.1) finally gives

$$-D_{\text{eff}}\frac{\partial^2 c}{\partial r^2}-D_{\text{eff}}\frac{1}{r}\frac{\partial c}{\partial r}+\frac{\partial \phi}{\partial t}c+\phi\frac{\partial c}{\partial t}+\frac{\partial s}{\partial t}=0. \tag{A.2}$$

Field Eq. (A.2) is supplemented by initial conditions $c(r,0)=c_0(r)$ and boundary conditions at the inner and the outer surface of the considered body, i.e., at $r=r_1$ and $r=r_{n+1}$. At each boundary, either the concentration in the pore fluid or the ionic flux $q_n=q\ n=-D_{\text{eff}}\partial c/\partial r\ n$, where $n$ is the outward normal on the surface, can be prescribed, i.e.,

$$\begin{aligned} &c_1=\bar{c}_1 \text{ on } S_c \quad \text{or} \quad D_{\text{eff}}\frac{\partial c}{\partial r}\Big|_{r_1}=\bar{q}_1 \text{ on } S_q,\\ &c_{n+1}=\bar{c}_{n+1} \text{ on } S_c \quad \text{or} \quad -D_{\text{eff}}\frac{\partial c}{\partial r}\Big|_{r_{n+1}}=\bar{q}_{n+1} \text{ on } S_q. \end{aligned} \tag{A.3}$$

In Eq. (A.3), $n_1$ and $n_{n+1}$ were set equal to $-1$ and $+1$, respectively; $\bar{q}$ is a prescribed ionic flux.

*Weak formulation and discretization in space and time*

Introducing an arbitrary virtual (continuous) concentration field $\delta c$ such that $\delta c=0$ on $S_c$, a weak form of the differential Eq. (A.2) and the boundary conditions (A.3) is obtained as

$$\begin{aligned} &\int_{r_1}^{r_{n+1}}\delta c\left[-D_{\text{eff}}\frac{\partial^2 c}{\partial r^2}-D_{\text{eff}}\frac{1}{r}\frac{\partial c}{\partial r}+\frac{\partial \phi}{\partial t}c+\phi\frac{\partial c}{\partial t}+\frac{\partial s}{\partial t}\right](2\pi r)dr\\ &+\delta c_1\left[-D_{\text{eff}}\frac{\partial c}{\partial r}\Big|_{r_1}+\bar{q}_1\right](2\pi r_1)+\delta c_{n+1}\left[D_{\text{eff}}\frac{\partial c}{\partial r}\Big|_{r_{n+1}}+\bar{q}_{n+1}\right](2\pi r_{n+1})=0. \end{aligned} \tag{A.4}$$

Integration by parts of the first term in Eq. (A.4) results in

$$\begin{aligned} &-2\pi\int_{r_1}^{r_{n+1}}(r\delta c)D_{\text{eff}}\frac{\partial^2 c}{\partial r^2}dr=\\ &-2\pi(r_{n+1}\delta c_{n+1})D_{\text{eff}}\frac{\partial c}{\partial r}\Big|_{r_{n+1}}+2\pi(r_1\delta c_1)D_{\text{eff}}\frac{\partial c}{\partial r}\Big|_{r_1}\\ &+2\pi\int_{r_1}^{r_{n+1}}\delta c\,D_{\text{eff}}\frac{\partial c}{\partial r}dr+2\pi\int_{r_1}^{r_{n+1}}r\frac{\partial \delta c}{\partial r}D_{\text{eff}}\frac{\partial c}{\partial r}dr. \end{aligned} \tag{A.5}$$

Inserting Eq. (A.5) into Eq. (A.4) gives

$$\begin{aligned} &\int_{r_1}^{r_{n+1}}\left[\frac{\partial(\delta c)}{\partial r}D_{\text{eff}}\frac{\partial c}{\partial r}+\delta c\frac{\partial \phi}{\partial t}c+\delta c\phi\frac{\partial c}{\partial t}+\delta c\frac{\partial s}{\partial t}\right](2\pi r)dr+\delta c_1\bar{q}_1(2\pi r_1)\\ &+\delta c_{n+1}\bar{q}_{n+1}(2\pi r_{n+1})=0. \end{aligned} \tag{A.6}$$

Discretization in space ($c=\mathbf{N}\mathbf{v}$, giving $\Delta c=\mathbf{N}\Delta\mathbf{v}$ and $\delta c=\mathbf{N}\delta\mathbf{v}$) and time ($\partial c/\partial t\to\Delta c/\Delta t$, $\partial\phi/\partial t\to\Delta\phi/\Delta t$, and $\partial s/\partial t\to\Delta s/\Delta t$) gives

$$\delta\mathbf{v}^T\left(\mathbf{R}_D+\mathbf{R}_\phi+\mathbf{R}_s+\mathbf{R}_{\text{bc}}\right)=0 \tag{A.7}$$

with

$$\mathbf{R}_D=\left[\mathop{\mathbf{A}}_{e=1}^{n}\int_{r_e}^{r_{e+1}}\left(\frac{\partial \mathbf{N}^T}{\partial r}D_{\text{eff}}\frac{\partial \mathbf{N}}{\partial r}\right)(2\pi r)dr\right]\mathbf{v},$$

$$\mathbf{R}_\phi=\left[\mathop{\mathbf{A}}_{e=1}^{n}\int_{r_e}^{r_{e+1}}\left(\mathbf{N}^T\frac{\Delta\phi}{\Delta t}\mathbf{N}\right)(2\pi r)dr\right]\mathbf{v}+\left[\mathop{\mathbf{A}}_{e=1}^{n}\int_{r_e}^{r_{e+1}}\left(\mathbf{N}^T\frac{\phi}{\Delta t}\mathbf{N}\right)(2\pi r)dr\right]\Delta\mathbf{v},$$

$$\mathbf{R}_s=\left[\mathop{\mathbf{A}}_{e=1}^{n}\int_{r_e}^{r_{e+1}}\left(\mathbf{N}^T\frac{\Delta s}{\Delta t}\right)(2\pi r)dr\right],$$

$$\mathbf{R}_{\text{bc}}=1_1\bar{q}_1(2\pi r_1)+1_{n+1}\bar{q}_{n+1}(2\pi r_{n+1}). \tag{A.8}$$

In Eq. (A.8), $1_1$ and $1_{n+1}$ are auxiliary vectors with $n+1$ components given by $1_1^T=\lfloor 1,0,0,\rfloor$ and $1_{n+1}^T=\lfloor 0,0,1\rfloor$. $\mathbf{R}_D+\mathbf{R}_\phi+\mathbf{R}_s+\mathbf{R}_{\text{bc}}=0$ is solved for discrete time instants by means of a standard incremental-iterative solution strategy [64,65],

$$\mathbf{R}^{(k)}+\frac{d\mathbf{R}}{d\mathbf{v}}\Big|^{(k)}\Delta\mathbf{v}^{(k+1)}=0, \tag{A.9}$$

where $(k)$ is the number of the iteration step and the consistent tangent is given as

$$\begin{aligned} \frac{d\mathbf{R}}{d\mathbf{v}}\Big|^{(k)}=&\mathop{\mathbf{A}}_{e=1}^{n}\int_{r_e}^{r_{e+1}}\left(\frac{\partial \mathbf{N}^T}{\partial r}D_{\text{eff}}\frac{\partial \mathbf{N}}{\partial r}\right)(2\pi r)dr\\ &+\mathop{\mathbf{A}}_{e=1}^{n}\int_{r_e}^{r_{e+1}}\left(\mathbf{N}^T\frac{\Delta\phi}{\Delta t}\mathbf{N}\right)(2\pi r)dr\\ &+\mathop{\mathbf{A}}_{e=1}^{n}\int_{r_e}^{r_{e+1}}\left(\mathbf{N}^T\frac{\phi}{\Delta t}\mathbf{N}\right)(2\pi r)dr\\ &+\mathop{\mathbf{A}}_{e=1}^{n}\int_{r_e}^{r_{e+1}}\left(\mathbf{N}^T\frac{1}{\Delta t}\frac{ds}{dc}\Big|^{(k)}\mathbf{N}\right)(2\pi r)dr. \end{aligned} \tag{A.10}$$

Note: for 1D dissolution/diffusion along the spatial coordinate $x$, the terms $(2\pi r)$, $(2\pi r_1)$, and $(2\pi r_{n+1})$ in Eqs. (A.8) and (A.10) are replaced by 1, and $\int_{r_e}^{r_{e+1}}\cdots dr$ is replaced by $\int_{x_e}^{x_{e+1}}\cdots dx$.

*Extension towards kinetics law for the dissolution process*

Recently, a dissolution kinetics law (using considerations from [18]) was proposed in [34,35], where the equilibrium function $\tilde{s}=\tilde{s}(c)$ serves as the limiting dissolution state. According to [34], the kinetics law reads

$$\frac{\partial s}{\partial t}=\frac{1}{\tau}\frac{\overline{T}}{T}ln\frac{c}{\tilde{c}} \tag{A.11}$$

with $\tau$ denoting the characteristic time of micro-diffusion of calcium in the pore systems, $\overline{T}$ is the reference temperature of 288 K and $\tilde{c}=\tilde{c}(s)$ is the inverted equilibrium function given, e.g., in Fig. 12. In [34] different characteristic times for the individual calcium bearing hydration products were used; in this paper, however, a single characteristic time is employed. The term $ds/dc$ required within the incremental-iterative solution strategy (Eq. (A.10)), previously determined directly from the equilibrium function $\tilde{s}(c)$, is now determined from time discretization of the kinetics law for the $(m+1)$-st time step $\Delta t_{m+1}=t_{m+1}-t_m$, using $\partial s/\partial t\to\Delta s/\Delta t$:

$$\mathcal{G}(s,c)=-\frac{\Delta s_{m+1}}{\Delta t_{m+1}}+\frac{1}{\tau}\frac{\overline{T}}{T}ln\frac{c_{m+1}}{\tilde{c}_{m+1}(s_{m+1})}=0; \tag{A.12}$$

$$\begin{aligned} \mathcal{G}(s,c)=0 \iff & d\mathcal{G}=\frac{\partial \mathcal{G}}{\partial c}dc+\frac{\partial \mathcal{G}}{\partial s}ds=0\\ \iff & \frac{ds}{dc}=-\frac{\partial \mathcal{G}}{\partial c}\left(\frac{\partial \mathcal{G}}{\partial s}\right)^{-1}\\ \iff & \frac{ds}{dc}=\frac{\frac{1}{\tau}\frac{\overline{T}}{T}\frac{1}{c_{m+1}}}{\frac{1}{\Delta t_{m+1}}+\frac{1}{\tau}\frac{\overline{T}}{T}\frac{1}{\tilde{c}_{m+1}}\frac{\partial \tilde{c}_{m+1}}{\partial s_{m+1}}}. \end{aligned} \tag{A.13}$$

## Appendix B. Notation, intrinsic material parameters, and constants used in paper

The following symbols are used in the paper:

| | |
|---|---|
| $1$ | auxiliary vector; |
| $a$ | fitting parameter in [12], ionic radius; |
| $A$, $B$ | parameters in Debye–Hückel–Onsager theory, parameters in function describing temperature dependency of viscosity; |
| $\mathbf{A}$ | assembly operator; |
| $c$ | calcium concentration in pore solution, molar concentration of electrolyte; |
| $\bar{c}$ | prescribed calcium concentration in pore solution, |
| $\tilde{c}$ | equilibrium material function for $c$ when dissolution kinetics law is used; |
| $c_0$ | initial calcium concentration in pore solution, |
| $c^{\mathrm{eq}}$ | equilibrium calcium concentration of solution saturated in CH; |
| $\mathbf{D}_{\mathrm{eff}}$ | effective diffusion tensor; |
| $D$ | diffusion coefficient for isotropic behavior; |
| $D_+^0$, $(D_-^0)$ | limiting diffusion coefficient of cation (anion) for ion concentration approaching zero; |
| $D_{\mathrm{eff}}$ | effective diffusion coefficient for isotropic behavior; |
| $D_{\mathrm{sol}}$ | diffusion coefficient in interstitial pore solution; |
| $D_{\mathrm{sol}}^0$ | electrolyte diffusion coefficient for ion concentration approaching zero; |
| $\overline{D}$ | fitting parameter in [12]; |
| $e$ | elementary charge; |
| $E$ | Young's modulus; |
| $E_{\mathrm{eff}}$ | effective Young's modulus; |
| $E_{\mathrm{m}}$ | Young's modulus of matrix material; |
| $F$ | Faraday constant; |
| $f_{\mathrm{C-S-H}}$ | volume fraction of C–S–H; |
| $f_{\mathrm{ett}}$ | volume fraction of ettringite; |
| $f_{\mathrm{m}}$ | volume fraction of matrix material; |
| $f_{\mathrm{mono}}$ | volume fraction of monosulfate; |
| $\mathbf{I}$ | (second-order) unity tensor; |
| $k$ | Boltzmann constant; number of iteration step |
| $K$ | constant in Kohlrausch's law; |
| $m_{\mathrm{CH}}$ | CH mass fraction; |
| $\mathcal{M}_{\mathrm{CH}}$ | molar weight of CH; |
| $n$ | outward normal; |
| $n$, $n+1$ | number of elements, number of nodes; |
| $m$ | time step of incremental analysis scheme; |
| $N$ | Avogadro number |
| $\mathbf{N}$ | matrix of shape functions |
| $q$ | constant dependent on symmetry/asymmetry of electrolyte; |
| $\mathbf{q}$, $q$ | molar flux; |
| $\bar{q}$ | prescribed molar flux; |
| $r$ | radial coordinate; |
| $R$ | universal gas constant; |
| $\mathbf{R}_{\mathrm{x}}$ | residuum vector; |
| $s$ | (apparent) calcium concentration bound in solid skeleton; |
| $\tilde{s}$ | equilibrium material function for $s$ when dissolution kinetics law is used; |
| $s^0$ | initial (apparent) calcium concentration bound in solid skeleton; |
| $s_{\mathrm{CH}}^0$ | (apparent) calcium concentration from CH bound in solid skeleton; |
| $s_{\mathrm{C-S-H}}^0$ | (apparent) calcium concentration from C–S–H bound in solid skeleton; |
| $S_c$ | boundary with prescribed calcium concentration in pore fluid; |
| $S_q$ | boundary with prescribed ionic flux; |
| $t$ | time; |
| $T$ | temperature; |
| $\overline{T}$ | reference temperature; |
| $T_\phi$ | tortuosity; |
| $u_+$, $(u_-)$ | ionic mobility of cation (anion); |
| $\mathbf{v}$ | vector of nodal concentrations; |
| $w/c$ | water/cement mass ratio; |
| $x$ | spatial coordinate; |
| $z_+$, $(z_-)$ | elementary charge of cation (anion); |
| $\alpha$ | function describing concentration dependency of molar conductivity; |
| $\delta c$ | virtual concentration field; |
| $\Delta\rho_{\mathrm{C-S-H}}$ | density decrease of C–S–H gel due to oven drying; |
| $\Delta\rho_{\mathrm{exp}}$ | experimentally determined density decrease; |
| $\epsilon$ | electric permittivity of water; |
| $\epsilon_0$ | vacuum permittivity; |
| $\epsilon_{\mathrm{rel}}$ | relative permittivity; |
| $\eta$ | viscosity of water; |
| $\kappa$ | conductivity of electrolyte solution; |
| $\overline{\kappa}$ | parameter in Debye–Hückel–Onsager theory; |
| $\lambda_+^0$, $(\lambda_-^0)$ | limiting molar conductivity of cation (anion) for zero ion concentration; |
| $\Lambda_{\mathrm{m}}$ | molar conductivity of electrolyte solution; |
| $\Lambda_{\mathrm{m}}^0$ | limiting molar conductivity for zero electrolyte concentration; |
| $\nu_{\mathrm{m}}$ | Poisson's ratio of matrix material; |
| $\nu_+$, $(\nu_-)$ | number of cations (anions) per stoichiometric unit of electrolyte; |
| $\rho$ | density; |
| $\rho_{\mathrm{H}}$ | density of water; |
| $\tau$ | characteristic time; |
| $\phi$ | pore space; |
| $\phi_{\mathrm{CH}}^{\mathrm{max}}$ | additional pore space due to complete CH dissolution; |
| $\phi_{\mathrm{C-S-H}}^{\mathrm{max}}$, $\bar{\phi}_{\mathrm{C-S-H}}^{\mathrm{max}}$ | additional pore space due to complete C–S–H decalcification, scaled to volume fraction of C–S–H; |
| $\phi_{\mathrm{cap}}$ | initial capillary pore space; |

**Table B.4**
Density $\rho$ and molar mass $\mathcal{M}$ of the different phases in Portland cement paste (taken from [40]).

| | | Density $\rho$ | Molar mass $\mathcal{M}$ |
|---|---|---|---|
| | | [kg/m$^3$] | [kg/mol] |
| Tricalcium silicate | $C_3S$ | 3150 | 0.228 |
| Dicalcium silicate | $C_2S$ | 3280 | 0.172 |
| Tricalcium aluminate | $C_3A$ | 3030 | 0.270 |
| Tetracalcium aluminate ferrite | $C_4AF$ | 3730 | 0.486 |
| Water | H | 998 | 0.018 |
| Gypsum | $C\bar{S}H_2$ | 2320 | 0.172 |
| Calcium hydroxide | CH | 2240 | 0.074 |
| Hydrogarnet | $C_3(A,F)H_6$ | 2670 | 0.407 |
| Trisulfate ettringite (saturated) | $C_6A\bar{S}_3H_{32}$ | 1750 | 1.255 |
| Monosulfate (saturated) | $C_4A\bar{S}H_{12}$ | 1990 | 0.623 |
| Calcium aluminate hydrate | $C_4AH_{13}$ | 2050 | 0.560 |
| Calcium silicate hydrate (saturated) | $C_{3.4}S_2H_8$ | 1990 | 0.454 |

**Table B.5**
Elementary constants appearing in derivation.

| Constant | Unit | Description |
|---|---|---|
| $F = 9.64853 \times 10^4$ | [C/mol] | Faraday constant |
| $R = 8.31451$ | [J/(K mol)] | Universal gas constant |
| $N = 6.02214 \times 10^{23}$ | [–] | Avogadro number |
| $k = 1.380650 \times 10^{-23}$ | [J/K] | Boltzmann constant |
| $e = 1.602177 \times 10^{-19}$ | [C] | Elementary charge |
| $\epsilon_0 = 8.85419 \times 10^{-12}$ | [C$^2$/(J m)] | Vacuum permittivity |

Conversion of units/constants:

1 C(oulomb) = 1 A s
1 S(iemens) = 1 s$^3$A$^2$/(m$^2$kg)
1 J = 1 m$^2$kg/s$^2$
1 C$^2$/(J S) = 1 s
$k = R/N$, $F = Ne$.

**Table B.6**
Relative permittivity of water [66].

| $T$ [°C] | $\epsilon_{rel}$ [−] |
|---|---|
| 0 | 87.90 |
| 10 | 83.95 |
| 20 | 80.18 |
| 30 | 76.58 |
| 40 | 73.15 |
| 50 | 69.88 |
| 60 | 66.76 |

## References


[1] F.-J. Ulm, E. Lemarchand, F.H. Heukamp, Elements of chemomechanics of calcium leaching of cement-based materials at different scales, Eng. Fract. Mech. 70 (2003) 871–889.
[2] F.H. Heukamp, F.-J. Ulm, J.T. Germaine, Mechanical properties of calcium-leached cement pastes. Triaxial stress states and the influence of the pore pressure, Cem. Concr. Res. 31 (2001) 767–774.
[3] F.-J. Ulm, G. Constantinides, F.H. Heukamp, Is concrete a poromechanics material? — a multiscale investigation or poroelastic properties, Mater. Struct. 37 (2004) 43–58.
[4] F. Adenot, M. Buil, Modelling of the corrosion of the cement paste by deionized water, Cem. Concr. Res. 22 (1992) 489–496.
[5] B. Gérard, Contribution des couplages mécanique-chimie-transfert dans la tenue a long terme des ouvrages de stockage de déchets radioactifs, Ph.D. thesis, Laboratoire de Méchanique et Technologie, E.N.S. de Cachan, in French (1996).
[6] B. Gérard, G. Pijaudier-Cabot, C. Laborderie, Coupled diffusion-damage modelling and the implications on failure due to strain localisation, Int. J. Solids Struct. 35 (31–32) (1998) 4107–4120.
[7] A. Delagrave, B. Gérard, J. Marchand, Modelling the calcium leaching mechanisms in hydrated cement pastes, in: K. Srivener, J. Young (Eds.), Mechanics of Chemical Degradation of Cement-Based Systems, Chapman & Hall, London, 1997, pp. 30–37.
[8] C. Carde, R. François, Modelling the loss of strength and porosity increase due to the leaching of cement pastes, Cem. Concr. Compos. 21 (3) (1999) 181–188.
[9] C. Carde, R. François, Effect of the leaching of calcium hydroxide from cement paste on mechanical and physical properties, Cem. Concr. Res. 27 (4) (1997) 539–550.
[10] C. Carde, R. François, J.-M. Torrenti, Leaching of both calcium hydroxide and C–S–H from cement paste: modeling the mechanical behavior, Cem. Concr. Res. 26 (8) (1996) 1257–1268.
[11] G. Pijaudier-Cabot, B. Gérard, L. Molez, Damage mechanics of concrete structures subjected to mechanical and environmental actions, in: R. de Borst, N. Bicanic, H.A. Mang, G. Meschke (Eds.), Computational Modelling of Concrete Structures, Balkema, Rotterdam, 1998, pp. 559–566.
[12] M. Mainguy, O. Coussy, Progagation fronts during calcium leaching and chloride penetration, J. Eng. Mech. (ASCE) 126 (3) (2000) 250–257.
[13] M. Mainguy, C. Tognazzi, J.-M. Torrenti, F. Adenot, Modelling of leaching in pure cement paste and mortar, Cem. Concr. Res. 30 (1) (2000) 83–90.
[14] M. Mainguy, F.J. Ulm, F.H. Heukamp, Coupled diffusion–dissolution around a fracture channel: the solute congestion phenomenon, Int. J. Transp. Porous Media 6 (2000) 1–19.
[15] M. Mainguy, F.J. Ulm, F.H. Heukamp, Similarity properties of demineralization and degradation of cracked porous materials, Int. J. Solids Struct. 38 (40–41) (2001) 7079–7100.
[16] C. Le Bellégo, B. Gérard, G. Pijaudier-Cabot, Chemo-mechanical effects in mortar beams subjected to water hydrolysis, J. Eng. Mech. 126 (3) (2000) 266–272.
[17] C. Le Bellégo, G. Pijaudier-Cabot, B. Gérard, J.-F. Dubé, L. Molez, Coupled mechanical and chemical damage in calcium leached cementitious structures, J. Eng. Mech. 129 (3) (2003) 333–341.
[18] F.-J. Ulm, J.-M. Torrenti, F. Adenot, Chemoporoplasticity of calcium leaching in concrete, J. Eng. Mech. (ASCE) 125 (1999) 1200–1211.
[19] F.H. Heukamp, F.-J. Ulm, J.T. Germaine, Does calcium leaching increase ductility of cementitious materials? Evidence from direct tensile tests, J. Mater. Civ. Eng. (ASCE) 17 (3) (2005) 307–312.
[20] D. Kuhl, F. Bangert, G. Meschke, Coupled chemo-mechanical deterioration of cementitious materials. Part I: modeling, Int. J. Solids Struct. 41 (1) (2004) 15–40.
[21] D. Kuhl, F. Bangert, G. Meschke, Coupled chemo-mechanical deterioration of cementitious materials. Part II: numerical methods and simulations, Int. J. Solids Struct. 41 (1) (2004) 41–67.
[22] V.H. Nguyen, B. Nedjar, H. Colina, J.M. Torrenti, A seperation of scales homogenization analysis for the modelling of calcium leaching in concrete, Comput. Methods Appl. Mech. Eng. 195 (2006) 7196–7210.
[23] J. Jain, N. Neithalath, Analysis of calcium leaching behavior of plain and modified cement pastes in pure water, Cem. Concr. Compos. 31 (3) (2009) 176–185.
[24] T. Rougelot, N. Burlion, D. Bernard, F. Skoczylas, About microcracking due to leaching in cementitious composites: X-ray microtomography description and numerical approach, Cem. Concr. Res. 40 (2) (2010) 271–283.
[25] T. de Larrard, F. Benboudjema, J. Colliat, J. Torrenti, F. Deleruyelle, Concrete calcium leaching at variable temperature: Experimental data and numerical model inverse identification, Comput. Mater. Sci. 49 (1) (2010) 35–45.
[26] L. Dormieux, E. Lemarchand, Homogenization approach of advection and diffusion in cracked porous material, ASCE J. Eng. Mech. 127 (12) (2001) 1267–1274.
[27] P. Pivonka, C. Hellmich, D. Smith, Microscopic effects on chloride diffusivity of cement pastes — a scale-transition analysis, Cem. Concr. Res. 34 (2004) 2251–2260.
[28] B.H. Oh, S.Y. Jang, Prediction of diffusivity of concrete based on simple analytic equations, Cem. Concr. Res. 34 (3) (2004) 463–480.
[29] B. Bary, S. Béjaoui, Assessment of diffusive and mechanical properties of hardened cement pastes using a multi-coated sphere assemblage model, Cem. Concr. Res. 36 (2) (2006) 245–258.
[30] S. Béjaoui, B. Bary, Modeling of the link between microstructure and effective diffusivity of cement pastes using a simplified composite model, Cem. Concr. Res. 37 (3) (2007) 469–480.
[31] E. Stora, Q.-C. He, B. Bary, A mixed composite spheres assemblage model for the transport properties of random heterogeneous materials with high contrasts, J. Appl. Phys. 100 (8) (2006) 084910.
[32] E. Stora, B. Bary, Q.-C. He, On estimating the effective diffusive properties of hardened cement pastes, Transp. Porous Media 73 (2008) 279–295.
[33] U.R. Berner, Evolution of pore water chemistry during degradation of cement in a radioactive waste repository environment, Waste Manage. 12 (2–3) (1992) 201–219.
[34] D. Gawin, F. Pesavento, B.A. Schrefler, Modeling of cementitious materials exposed to isothermal calcium leaching, considering process kinetics and advective flow. Part 1: Theoretical model, Int. J. Solids Struct. 45 (2008) 6221–6240.
[35] D. Gawin, F. Pesavento, B.A. Schrefler, Modeling of cementitious materials exposed to isothermal calcium leaching, considering process kinetics and advective flow. Part 2: Numerical solution, Int. J. Solids Struct. 45 (2008) 6241–6268.
[36] D. Gawin, F. Pesavento, B.A. Schrefler, Modeling deterioration of cementitious materials exposed to calcium leaching in non-isothermal conditions, Comput. Methods Appl. Mech. Eng. 198 (37–40) (2009) 3051–3083.
[37] J.J. Chen, J.J. Thomas, H.F.W. Taylor, H.M. Jennings, Solubility and structure of calcium silicate hydrate, Cem. Concr. Res. 34 (9) (2004) 1499–1519 H. F. W. Taylor Commemorative Issue.
[38] L. Dormieux, D. Kondo, F.-J. Ulm, Microporomechanics, Wiley, Chichester, 2006.
[39] D. Gross, T. Seelig, Bruchmechanik, mit einer Einführung in die Mikromechanik (Fracture mechanics, containing an introduction to continuum micromechanics), Springer, 2001 in German.
[40] P.D. Tennis, H.M. Jennings, A model for two types of calcium silicate hydrate in the microstructure of Portland cement pastes, Cem. Concr. Res. 30 (2000) 855–863.
[41] C. Pichler, R. Lackner, H.A. Mang, A multiscale micromechanics model for the autogenous-shrinkage deformation of early-age cement-based materials, Eng. Fract. Mech. 74 (1–2) (2007) 34–58.
[42] H.M. Jennings, A model for the microstructure of calcium silicate hydrate in cement paste, Cem. Concr. Res. 30 (2000) 101–116.
[43] H.M. Jennings, Colloid model of C–S–H and implications to the problem of creep and shrinkage, Mater. Struct. 37 (2004) 59–70.
[44] J.J. Thomas, H.M. Jennings, A colloidal interpretation of chemical aging of C–S–H gel and and its effects on the properties of cement paste, Cem. Concr. Res. 36 (2006) 30–38.
[45] H.M. Jennings, Refinements to colloid model of C–S–H in cement: CM-II, Cem. Concr. Res. 38 (2008) 275–289.
[46] T. Mori, K. Tanaka, Average stress in matrix and average elastic energy of materials with misfitting inclusions, Acta Metall. 21 (1973) 571–574.
[47] A.V. Hershey, The elasticity of an isotropic aggregate of anisotropic cubic crystals, J. Appl. Mech. (ASME) 21 (1954) 236–240.
[48] E. Kroener, Berechnung der elastischen Konstanten des Vielkristalls aus den Konstanten des Einkristalls, Z. Phys. 151 (1958) 504–518 in German.
[49] A. Zaoui, Structural morphology and constitutive behaviour of microheterogeneous materials, in: P. Suquet (Ed.), Continuum Micromechanics, CISM Courses and Lectures, 377, Springer, Vienna, 1997.
[50] G. Constantinides, F.-J. Ulm, The effect of two types of C–S–H on the elasticity of cement-based materials: results from nanoindentation and micromechanical modeling, Cem. Concr. Res. 34 (2004) 67–80.
[51] R.M. Christensen, K.H. Lo, Solutions for the effective shear properties in three phase sphere and cylinder models, J. Mech. Phys. Solids 27 (1979) 315–330.
[52] R.M. Christensen, K.H. Lo, Erratum. Solutions for the effective shear properties in three phase sphere and cylinder models, J. Mech. Phys. Solids 34 (1986) 639.
[53] P. Atkins, Physical Chemistry, 5th Edition Oxford University Press, New York, 1994.
[54] C.H. Hamann, A. Hamnett, W. Vielstich, Electrochemistry, 2nd Edition Wiley-VCH, Weinheim, 2007.
[55] R.A. Robinson, R.H. Stokes, Electrolyte Solutions, Butterworth, 1959.
[56] H.J. De Wane, W.J. Hamer, Electrochical data, Part X. Electrolytic conductivity of aqueous solutions of the alkali metal hydroxides, Tech. rep., National Bureau of Standards Report 9876, U.S. Department of Commerce, 1970.
[57] P. Vanýsek, Electrochemical series, Handbook of Chemistry and Physics, Chemical Rubber Company, 2000.
[58] J. Newman, Electrochemical Systems, Prentice-Hall, Englewood Cliffs, NJ, USA, 1991.
[59] J.J. Chen, J.J. Thomas, H.M. Jennings, Decalcification shrinkage of cement paste, Cem. Concr. Res. 36 (5) (2006) 801–809.
[60] C. Carde, G. Escadeillas, R. François, Use of ammonium nitrate solution to simulate and accelerate the leaching of cement pastes due to deionized water, Mag. Concr. Res. 49 (181) (1997) 295–301.
[61] Y. Ichikawa, K. Kawamura, N. Fujii, T. Nattavut, Molecular dynamics and multiscale homogenization analysis of seepage/diffusion problem in bentonite clay, Int. J. Numer. Methods Eng. 54 (2002) 1717–1749.

[62] J.J. Thomas, J.J. Chen, A.J. Allen, H.M. Jennings, Effects of decalcification on the microstructure and surface area of cement and tricalcium silicate pastes, Cem. Concr. Res. 34 (12) (2004) 2297–2307.
[63] H.M. Jennings, J.J. Thomas, J.S. Gevrenov, G. Constantinides, F.-J. Ulm, A multitechnique investigation of the nanoporosity of cement paste, Cem. Concr. Res. 37 (3) (2007) 329–336.
[64] K.-J. Bathe, Finite Element Procedures, Prentice-Hall, Englewood Cliffs, New Jersey, USA, 1996.
[65] O.C. Zienkiewicz, R.L. Taylor, J.Z. Zhu, The Finite Element Methods: Its Basics and Fundamentals, Elsevier, Oxford, 2005.
[66] N.E. Hill, The temperature dependence of the dielectric properties of water, J. Phys. C: Solid State Phys. 3 (1970) 238–239.